

Holographic QCD equation of state constrained by lattice QCD: neural-ODE for probe-limit and a back-reaction test

Yutian Deng,^{1,2,*} Mei Huang,^{3,†} and Lin Zhang^{1,2,‡}

¹*School of Science, Shenzhen Campus of Sun Yat-sen University, No. 66, Gongchang Road, Guangming District, Shenzhen, Guangdong 518107, P. R. China*

²*Sun Yat-sen University, No. 135, Xingang Xi Road, Guangzhou, Guangdong 510275, P. R. China*

³*School of Nuclear Science and Technology, University of Chinese Academy of Sciences, Beijing, 100049, P. R. China*

We study the equation of state (EoS) of QCD matter in a bottom-up holographic setup that combines an Einstein-Maxwell-dilaton (EMD) sector with an improved Karch-Katz-Son-Stephanov (KKSS) flavor action. In the probe approximation, we perform an inverse reconstruction of the model functions by parameterizing them with neural networks and solving the EMD equations via a differentiable ODE solver (a neural ODE framework), calibrating the model to a $(2 + 1)$ -flavor lattice-QCD EoS at finite temperature and finite baryon chemical potential. The reconstructed model functions are then parametrized and kept fixed across thermodynamic states. Next, viewing the EMD sector as an effective description of pure Yang–Mills theory, we fix its parameters by fitting the $\mu_B = 0$ lattice pure-gluon EoS using a hybrid optimization strategy. Finally, we go beyond the probe limit and solve the coupled EMD+KKSS equations with back-reaction, using the pure-gluon-calibrated EMD sector as a fixed input and varying the KKSS couplings to compare with the $\mu_B = 0$ two-flavor lattice EoS. We find a visible mismatch and a high-temperature behavior in which the back-reacted dimensionless ratios approach a nearly β_1 -insensitive plateau close to the pure-gluon baseline, providing a simple structural diagnostic for the present flavor-sector truncation.

This article has been submitted to Chinese Physics C.

I. INTRODUCTION

Quantum chromodynamics (QCD) is believed to be the fundamental theory of the strong interaction. In regimes of interest for heavy-ion collisions and compact-star physics, the coupling is large and controlled calculations are scarce. Lattice QCD provides high-quality results for the equation of state (EoS) at finite temperature; see, e.g., Ref. [1] for a review. However, at finite baryon chemical potential μ_B , the sign problem limits direct simulations, which motivates effective descriptions that can be confronted with lattice data and extrapolated to finite density. For continuum perspectives at finite temperature and density, see, e.g., Ref. [2].

Based on the AdS/CFT correspondence [3], the holographic QCD method provides a useful non-perturbative approach to explore QCD matter under extreme conditions, e.g. finite temperature and/or baryon density, magnetic and vortical fields [4–25]. In bottom-up constructions, the Einstein–Maxwell–dilaton (EMD) framework is widely used, where the dilaton field provides an effective description of the gluodynamics and the model can be calibrated to lattice thermodynamics by choosing

the dilaton potential and the gauge kinetic function. To incorporate chiral physics and flavor dynamics in addition to the gluon sector, one usually supplements the EMD background with a flavor action containing a bulk scalar field dual to $\bar{q}q$, as in the hard-wall/soft-wall models [26, 27], and their improved variants for chiral symmetry breaking and restoration [28].

The original soft-wall model introduced by Andreas Karch, Emanuel Katz, Dam T. Son, and Mikhail A. Stephanov [27], often referred to as the Karch–Katz–Son–Stephanov (KKSS) model, provides a simple framework for light-flavor hadron spectra and chiral dynamics, and it also serves as a convenient starting point for improved soft-wall constructions. In many applications, the KKSS sector is treated as a probe: one first solves the EMD background and then evaluates the flavor contribution on top of it. This is efficient and often sufficient for qualitative studies. A more self-consistent description requires the back-reaction of the flavor sector on the geometry. In practice, solving the coupled EMD+KKSS system while keeping a single action fixed across thermodynamic states, and simultaneously calibrating to lattice EoS data, is technically nontrivial. As a result, systematic back-reacted studies remain comparatively limited. In particular, it is nontrivial to calibrate a coupled EMD+flavor setup to lattice thermodynamics while keeping a single five-dimensional action fixed across thermodynamic states. This motivates a controlled back-reaction study within a fixed EMD+KKSS action, which is one of the main focuses of this work.

In this work, we report three related studies within a single EMD+KKSS framework. We first work in the probe approximation and calibrate the EMD model to the lattice EoS of $(2 + 1)$ -flavor QCD at finite T and finite μ_B by using a neural ordinary differential equation

* Funding: start-up funding from Sun Yat-sen University (SYSU) (Y. Deng and L. Zhang); National Natural Science Foundation of China (NSFC) under Grant Nos. 12235016 (L. Zhang and M. Huang) and 12221005 (M. Huang); dengyt8@mail2.sysu.edu.cn

† huangmei@ucas.ac.cn

‡ zhanglin57@mail.sysu.edu.cn

(neural ODE) approach [21, 29–31], and subsequently fit the trained neural networks into explicit analytical expressions. We then treat the EMD system as an effective description of pure Yang–Mills theory and fix its parameters by fitting the $\mu_B = 0$ lattice pure-gluon EoS via a hybrid optimization strategy; see also recent data-driven Einstein–dilaton reconstructions of pure-gluon thermodynamics [32]. Finally, we go beyond the probe approximation and solve the coupled EMD+KKSS equations with back-reaction. With the EMD sector fixed by the pure-gluon calibration, we vary the KKSS couplings and compare the resulting $\mu_B = 0$ EoS with the two-flavor lattice data. A visible mismatch remains, which we view as a structural diagnostic for the present flavor-sector truncation. Moreover, by examining the high-temperature behavior, we find that the back-reacted dimensionless ratios approach a nearly β_1 -insensitive plateau close to the $\beta_1 = 0$ (pure-gluon) baseline, which provides a simple diagnostic for the present flavor-sector truncation.

This paper is organized as follows. In Sec. II we introduce the EMD+KKSS setup and the thermodynamic dictionary. In Sec. III we present the probe-approximation calibration for $(2 + 1)$ flavors at finite T and μ_B using neural ODE. In Sec. IV we present the pure-gluon calibration of the EMD sector at $\mu_B = 0$. In Sec. V we describe the coupled EMD+KKSS system with back-reaction and compare with the two-flavor $\mu_B = 0$ lattice EoS. We conclude and discuss outlook in Sec. VI.

II. THE HOLOGRAPHIC FRAMEWORK AND THE BACKGROUND SPACE-TIME OF THE HOLOGRAPHIC MODELS

Firstly we introduce the framework of the Einstein–Maxwell–dilaton (EMD) system, which reduces to the gravity–dilaton system at zero chemical potential. The EMD system is widely used in holographic QCD models. It can be used to describe the QCD confinement–deconfinement phase diagram [18, 19], the effect of the magnetic field on the QCD phase transition [20, 21], the rotating effect on the deconfinement phase transition [33, 34], the thermodynamic properties of QCD and the location of the critical endpoint (CEP) [22–25], the critical behavior near the CEP [35, 36], and the glueball spectra and corresponding EoS [32, 37]. Related bottom-up frameworks with dynamical flavors include the Einstein–dilaton–flavor (without a Maxwell sector) and the Einstein–Maxwell–Dilaton–flavor constructions, which have been applied to the 2+1-flavor QCD phase structure [38, 39].

Including the flavor sector, the total action of the 5-dimensional holographic QCD model is

$$S_{\text{total}}^s = S_{EMD}^s + S_f^s, \quad (1)$$

where S_{EMD}^s is the action for the EMD system in the string frame, and S_f^s is the action for the flavor part

(improved KKSS type) in the string frame. Some aspects of a similar model were reviewed in Ref. [40].

The EMD action in the string frame is denoted by S_{EMD}^s :

$$S_{EMD}^s = \frac{1}{2\kappa_5^2} \int d^5x \sqrt{-g^s} e^{-2\Phi} \left[R^s + 4g^{sMN} \partial_M \Phi \partial_N \Phi - V^s(\Phi) - \frac{h(\Phi)}{4} e^{\frac{4\Phi}{3}} g^{sMP} g^{sNQ} F_{MN} F_{PQ} \right], \quad (2)$$

where s denotes the string frame, $\kappa_5^2 = 8\pi G_5$, G_5 is the 5-dimensional Newton constant. g^s is the determinant of the metric in the string frame: $g^s = \det(g_{MN}^s)$. The metric tensor in the string frame can be extracted from

$$ds^2 = \frac{L^2 e^{2A_s(z)}}{z^2} \left(-f(z) dt^2 + \frac{dz^2}{f(z)} + dy_1^2 + dy_2^2 + dy_3^2 \right), \quad (3)$$

where L is the curvature radius of the asymptotic AdS_5 space-time. For simplicity and without loss of generality, we assume $L = 1$ in the following calculations. R^s is the Ricci curvature scalar in the string frame. The 5-dimensional scalar field $\Phi(z)$ is the dilaton field that depends only on the coordinate z . F_{MN} is the field strength of the $U(1)$ gauge field A_M :

$$F_{MN} = \partial_M A_N - \partial_N A_M. \quad (4)$$

The 5-dimensional vector field A_M is dual to the baryon number current. The function $h(\Phi)$ describes the gauge kinetic function and the function $V^s(\Phi)$ is the dilaton potential in the string frame. In this paper, to avoid confusion with the flavor-sector potential, we denote

$$V^s(\Phi) \equiv V_G^s(\Phi), \quad V^E(\Phi) \equiv V_G^E(\Phi), \quad (5)$$

and reserve V_X for the scalar potential of the KKSS sector.

A. The Einstein–Maxwell–dilaton system

As discussed in Ref. [41], it is more convenient to choose the string frame when solving the vacuum expectation value of the loop operator, and it is more convenient to choose the Einstein frame to work out the gravity solution and to study the equation of state. So we apply the following Weyl transformation [42, 43] to Eq. (2):

$$g_{MN}^s = e^{\frac{4}{3}\Phi} g_{MN}^E, \quad (6)$$

where g_{MN}^E is the metric tensor in the Einstein frame. The capital letter 'E' denotes the Einstein frame. Then, Eq. (2) becomes

$$S^E = \frac{1}{2\kappa_5^2} \int d^5x \sqrt{-g^E} \left[R^E - \frac{4}{3} g^{EMN} \partial_M \Phi \partial_N \Phi \right]$$

$$-V^E(\Phi) - \frac{h(\Phi)}{4} g^{EMP} g^{ENQ} F_{MNP} F_{PQ}], \quad (7)$$

where the function $V^E = e^{\frac{4}{3}\Phi} V^s$.

The coefficient of the kinetic term of the dilaton field Φ is $\frac{4}{3}$ in Eq. (7), which is not canonical. So we define a new dilaton field ϕ :

$$\phi = \sqrt{\frac{8}{3}} \Phi. \quad (8)$$

Now the action Eq. (7) becomes

$$S^E = \int d^5 \mathcal{L}^E, \quad (9)$$

where \mathcal{L}^E is the Lagrangian density in the Einstein frame:

$$\begin{aligned} \mathcal{L}^E = & \frac{1}{2\kappa_5^2} \sqrt{-g^E} \left[R^E - \frac{1}{2} g^{E MN} (\partial_M \phi) (\partial_N \phi) \right. \\ & \left. - V_\phi(\phi) - \frac{h_\phi(\phi)}{4} g^{E M \tilde{M}} g^{E N \tilde{N}} F_{M N} F_{\tilde{M} \tilde{N}} \right]. \end{aligned} \quad (10)$$

The function $V_\phi(\phi) = V^E(\Phi)$, and $h_\phi(\phi) = h(\Phi)$.

For asymptotically AdS solutions, the UV behavior of $V_\phi(\phi)$ is constrained by the scaling dimension Δ_ϕ of the operator dual to the dilaton ϕ . Expanding around $\phi \rightarrow 0$, one has

$$\begin{aligned} V_\phi(\phi) &= -\frac{12}{L^2} + \frac{1}{2} m_\phi^2 \phi^2 + \mathcal{O}(\phi^4), \\ m_\phi^2 L^2 &= \Delta_\phi(\Delta_\phi - 4), \end{aligned} \quad (11)$$

which is the usual AdS/CFT mass-dimension relation. In bottom-up holographic QCD, Δ_ϕ is treated as a phenomenological UV input: it controls how fast the background departs from AdS and thus encodes the nonconformality associated with the running coupling (or, equivalently, the trace anomaly), but it should not be identified with the perturbative QCD beta function. In this work we allow different Δ_ϕ in different calibration steps (e.g. $\Delta_\phi = 3.6$ in the probe reconstruction of Sec. III and $\Delta_\phi = 3.8$ in the pure-gluon/back-reacted study). These choices should be viewed as effective parameters optimized for the corresponding calibration targets and temperature windows, rather than as unique predictions derived from QCD in the UV. A more quantitative running-coupling-based justification would require scanning Δ_ϕ and refitting the model functions to the thermodynamic data, which we leave for a dedicated follow-up study.

According to Eqs. (3), (6) and (8), we then derive the line element of the space-time in the Einstein frame:

$$\begin{aligned} ds^2 = & \frac{L^2 e^{2A_E(z)}}{z^2} \left(-f(z) dt^2 + \frac{dz^2}{f(z)} + dy_1^2 \right. \\ & \left. + dy_2^2 + dy_3^2 \right), \end{aligned} \quad (12)$$

where

$$A_E(z) = A_s(z) - \sqrt{\frac{1}{6}} \phi(z). \quad (13)$$

Using the variation method, we can derive the Einstein field equations and the equations of motion of A_M and ϕ from the EMD action in Eqs. (9)–(10). It is noticed that these equations are obtained by neglecting the back-reaction from the flavor sector S_f^s ; otherwise, the field equations would involve additional source terms and become significantly more complex:

$$\begin{aligned} R_{MN}^E - \frac{1}{2} g_{MN}^E R^E - \frac{1}{2} T_{MN} &= 0, \\ \nabla_M [h_\phi(\phi) F^{MN}] &= 0, \\ \partial_M [\sqrt{-g} \partial^M \phi] - \sqrt{-g} \left(\frac{dV_\phi(\phi)}{d\phi} + \frac{F_E^2}{4} \frac{dh_\phi(\phi)}{d\phi} \right) &= 0, \end{aligned} \quad (14)$$

where $F_E^2 \equiv g^{EMP} g^{ENQ} F_{MNP} F_{PQ}$. where T_{MN} is the energy-momentum tensor:

$$\begin{aligned} T_{MN} = & (\partial_M \phi) (\partial_N \phi) - \frac{1}{2} g_{MN}^E g^{EPQ} (\partial_P \phi) (\partial_Q \phi) \\ & - g_{MN}^E V_\phi(\phi) + h_\phi(\phi) \left(g^{EPQ} F_{MP} F_{NQ} \right. \\ & \left. - \frac{1}{4} g_{MN}^E g^{EP\tilde{P}} g^{EQ\tilde{Q}} F_{PQ} F_{\tilde{P}\tilde{Q}} \right). \end{aligned} \quad (15)$$

We assume that all components of the vector field $A_M(z)$ vanish except the t -component $A_t(z)$. Substituting the metric in Eq. (12) into the equations of motion in Eq. (14), we obtain the EoMs for the background fields:

$$A_t'' + A_t' \left(-\frac{1}{z} + \frac{h_\phi'}{h_\phi} + A_E' \right) = 0, \quad (16)$$

$$f'' + f' \left(-\frac{3}{z} + 3A_E' \right) - \frac{e^{-2A_E} A_t'^2 z^2 h_\phi}{L^2} = 0, \quad (17)$$

$$A_E'' - A_E' \left(-\frac{2}{z} + A_E' \right) + \frac{\phi'^2}{6} = 0, \quad (18)$$

$$\begin{aligned} \phi'' + \phi' \left(-\frac{3}{z} + \frac{f'}{f} + 3A_E' \right) \\ - \frac{L^2 e^{2A_E}}{z^2 f} \frac{dV_\phi(\phi)}{d\phi} + \frac{z^2 e^{-2A_E} A_t'^2}{2L^2 f} \frac{dh_\phi(\phi)}{d\phi} = 0, \end{aligned} \quad (19)$$

$$\begin{aligned} A_E'' + \frac{f''}{6f} + A_E' \left(-\frac{6}{z} + \frac{3f'}{2f} \right) \\ - \frac{1}{z} \left(-\frac{4}{z} + \frac{3f'}{2f} \right) + 3A_E'^2 + \frac{L^2 e^{2A_E} V_\phi}{3z^2 f} = 0. \end{aligned} \quad (20)$$

Here and in the following, a prime denotes the derivative with respect to the holographic coordinate z . Only 4 equations are independent in the above 5 equations. So we choose Eq. (20) as a constraint and use it to check the solutions of the EoMs.

B. The flavor part action in the holographic model

As mentioned earlier, S_f^s in Eq. (1) describes the flavor part in the string frame. Here we use an improved KKSS action:

$$S_f^s = - \int d^5x \sqrt{-g^s} e^{-\Phi} \beta(\Phi) \times \text{Tr} \left\{ |D_M X|^2 + V_X^s(X, \Phi, F_s^2) + \frac{1}{4g_5^2} (F_L^2 + F_R^2) \right\} + S_{\text{baryons}}^s. \quad (21)$$

where

$$D_M X = \nabla_M X - ig_c A_M X \quad (22)$$

is the covariant derivative of the 5-dimensional scalar field X . In this work we keep the general polynomial form

$$V_X^s(X, \Phi, F_s^2) = \sum_{n=1}^2 \lambda_{2n} |X|^{2n}, \quad (23)$$

where $\lambda_2 \equiv M_{X_5}^2$ and $F_s^2 \equiv g^{sMP} g^{sNQ} F_{MN} F_{PQ}$. We remind the reader that in our convention the KKSS parameters λ_2 and λ_4 are precisely the coefficients entering Eq. (23), controlling the quadratic and quartic terms in V_X . Moreover, λ_2 is not a free parameter: it is fixed by the AdS/CFT mass-dimension relation for the bulk scalar X (see the discussion below leading to $M_{X_5}^2 = -3$), while λ_4 will be treated phenomenologically and tuned in the back-reacted $N_f = 2$ study. After the Weyl transformation in Eq. (6), the potential in the Einstein frame acquires an explicit dilaton dependence. In our convention,

$$V_X^E(X, \Phi, F_E^2) = e^{\frac{4}{3}\Phi} V_X^s(X, \Phi, e^{-\frac{8}{3}\Phi} F_E^2). \quad (24)$$

where $F_E^2 \equiv g^{EMP} g^{ENQ} F_{MN} F_{PQ}$. The function $\beta(\Phi)$ controls the coupling strength between the flavor part and the EMD background, and we use the following smooth ansatz:

$$\beta(\Phi) = \beta_1 \frac{\arctan(\beta_2 \Phi - \beta_3) + \frac{\pi}{2}}{\pi}, \quad (25)$$

where $(\beta_1, \beta_2, \beta_3)$ are model parameters. In this work, these parameters will be tuned in the comparison with the lattice EoS in the back-reacted $N_f = 2$ study; in particular, we will vary β_1 to assess the sensitivity to the overall strength of the flavor back-reaction. The original KKSS action is proposed in Ref. [27] and it is modified in Refs. [44–47] to describe the chiral phase transition and meson spectra.

According to the AdS/CFT dictionary [26], the bulk scalar field X and the chiral gauge fields $A_{L,R}^M$ are dual

to the relevant QCD operators at the ultraviolet (UV) boundary $z = 0$. The bulk scalar field X can be decomposed as

$$X = \left(\frac{\chi(z)}{2} + S(x, z) \right) e^{2i\pi(x, z)}, \quad (26)$$

where $\pi(x, z) = \pi^a(x, z)t^a$ is the pseudoscalar meson field and $S(x, z)$ is the scalar meson field. The field $\chi(z)$ is related to the vacuum expectation value (VEV):

$$\langle X \rangle = \frac{\chi}{2} I_2, \quad (27)$$

where I_2 is the 2×2 identity matrix. For the $N_f = 2$ flavor sector studied in this work, we assume the light quark masses are degenerate, which leads to the diagonal form $\chi \equiv \chi_u = \chi_d$. The 5-dimensional bulk gauge field $A_{L,R}^M$ can be recombined into the vector field V^M and the axial-vector field A^M :

$$V^M = \frac{1}{2}(A_L^M + A_R^M), \quad A^M = \frac{1}{2}(A_L^M - A_R^M). \quad (28)$$

The field-strength tensor for the vector field and the axial-vector field are

$$\begin{aligned} F_V^{MN} &= \frac{1}{2}(F_L^{MN} + F_R^{MN}) \\ &= \partial^M V^N - \partial^N V^M - i[V^M, V^N] - i[A^M, A^N], \\ F_A^{MN} &= \frac{1}{2}(F_L^{MN} - F_R^{MN}) \\ &= \partial^M A^N - \partial^N A^M - i[V^M, A^N] - i[A^M, V^N]. \end{aligned} \quad (29)$$

$$(30)$$

According to mass-dimension relationship $M^2 = (\Delta - p)(\Delta + p - 4)$ and $\Delta = 3, p = 0$, the 5-dimensional mass square of the bulk field X is $M_{X_5}^2 = -3$.

The action S_f^s that describes the flavor part can be decomposed as

$$S_f^s = S_\chi^s + S_{\text{mesons}}^s + S_{\text{baryons}}^s, \quad (31)$$

where

$$S_\chi^s = - \int d^5x \sqrt{-g^s} e^{-\Phi} \beta(\Phi) \left\{ \frac{1}{2} |\partial_M \chi - ig_c A_M \chi|^2 + \text{Tr}[V_X^s(\langle X \rangle, \Phi, F_s^2)] \right\} \quad (32)$$

After the Weyl transformation in Eq. (6), the corresponding action in the Einstein frame can be written as

$$S_\chi^E = - \int d^5x \sqrt{-g^E} e^\Phi \beta(\Phi) \left\{ \frac{1}{2} |\partial_M \chi - ig_c A_M \chi|_E^2 + \text{Tr}[V_X^E(\langle X \rangle, \Phi, F_E^2)] \right\}, \quad (33)$$

where $|\dots|_E^2 \equiv g^{EMN}(\dots)^\dagger(\dots)$ and V_X^E is defined in Eq. (24). Equation (33) is the action for the thermodynamic VEV $\chi(z)$. The 5-dimensional fields dual to the meson and baryon towers are treated as perturbations around this background. The contributions from S_{mesons}^s and S_{baryons}^s to the thermodynamics are expected to be subleading compared with that from S_χ^s , and thus we neglect them in the thermodynamic calculation in this article.

C. Coupled equations of motion with back-reaction

In the general case where the back-reaction of the flavor sector is considered, the fields $\{A_t, f, A_E, \phi, X\}$ are solved simultaneously as a coupled system. By varying the total action $S_{\text{total}}^E = S_{EMD}^E + S_\chi^E$, we can derive the complete Einstein field equations and the equations of motion for the gauge field A_M , the dilaton ϕ , and the scalar field X . Here we focus on the thermodynamic background and only consider the contribution from the vacuum expectation value (VEV) $\chi(z)$, while the fluctuations corresponding to meson and baryon excitations are neglected in the coupled equations. In tensor form, these equations are given by:

$$\frac{1}{16\pi G_5} \left[R_{MN}^E - \frac{1}{2} g_{MN}^E R^E - \frac{1}{2} T_{MN}^{EMD} \right] - \frac{1}{2} \beta(\Phi) e^\Phi T_{MN}^X = 0, \quad (34)$$

$$\begin{aligned} \partial_M \left[\sqrt{-g} \left(\frac{h_\phi}{16\pi G_5} \right. \right. \\ \left. \left. + 4e^\Phi \beta(\Phi) \frac{\partial}{\partial F_E^2} \left\{ \text{Tr} \left[V_X^E(\langle X \rangle, \Phi, F_E^2) \right] \right\} \right) \right. \\ \left. \times g^{EMP} g^{ENQ} F_{PQ} \right] \\ - 2\sqrt{-g} e^\Phi \beta(\Phi) g_c^2 g^{ENM} A_M \text{Tr} \left[\langle X \rangle^\dagger \langle X \rangle \right] = 0, \quad (35) \end{aligned}$$

$$\begin{aligned} \partial_M \left[\frac{\sqrt{-g}}{16\pi G_5} g^{EMN} \partial_N \phi \right] \\ - \frac{1}{16\pi G_5} \left(\sqrt{-g} \frac{dV_\phi}{d\phi} + \sqrt{-g} \frac{F_E^2}{4} \frac{dh_\phi}{d\phi} \right) \\ - \frac{\partial}{\partial \phi} \left\{ \sqrt{-g} \beta(\Phi) e^\Phi \text{Tr} \left[g^{EPQ} D_P \langle X \rangle^\dagger D_Q \langle X \rangle \right. \right. \\ \left. \left. + V_X^E(\langle X \rangle, \Phi, F_E^2) \right] \right\} \\ = 0, \quad (36) \end{aligned}$$

$$\begin{aligned} D_M \left(\sqrt{-g} \beta(\Phi) e^\Phi g^{EMN} D_N \langle X \rangle \right) \\ - \sqrt{-g} \beta(\Phi) e^\Phi \frac{\partial}{\partial \langle X \rangle^\dagger} \left\{ \text{Tr} \left[V_X^E(\langle X \rangle, \Phi, F_E^2) \right] \right\} = 0, \quad (37) \end{aligned}$$

where T_{MN}^{EMD} is defined in Eq. (15), and the general flavor energy-momentum tensor is defined using the trace

operator:

$$\begin{aligned} T_{MN}^X = \text{Tr} \left[(D_M \langle X \rangle)^\dagger D_N \langle X \rangle + (D_N \langle X \rangle)^\dagger D_M \langle X \rangle \right. \\ \left. - g_{MN}^E \left(g^{EPQ} (D_P \langle X \rangle)^\dagger D_Q \langle X \rangle \right. \right. \\ \left. \left. + V_X^E(\langle X \rangle, \Phi, F_E^2) \right) \right] \\ + 4 \frac{\partial \{ \text{Tr} [V_X^E(\langle X \rangle, \Phi, F_E^2)] \}}{\partial F_E^2} g^{EPQ} F_{MP} F_{NQ}. \quad (38) \end{aligned}$$

After substituting the metric ansatz into the above tensor equations, and following the style of Eqs. (16)–(19), we obtain the following complete set of back-reacted equations of motion for $N_f = 2$ flavors in the Einstein frame. To simplify the expressions, we define the effective gauge kinetic function as:

$$\mathcal{K}(z) \equiv h_\phi + 64\pi G_5 e^\Phi \beta(\Phi) \frac{\partial}{\partial F_E^2} \text{Tr} \left[V_X^E(\langle X \rangle, \Phi, F_E^2) \right]. \quad (39)$$

The coupled equations are given by:

$$\begin{aligned} A_t'' + A_t' \left(-\frac{1}{z} + A_E' + \frac{\mathcal{K}'}{\mathcal{K}} \right) \\ - \frac{16\pi G_5 L^2 e^{2A_E} \beta(\Phi) e^\Phi g_c^2 A_t \chi^2}{z^2 f \mathcal{K}} = 0, \quad (40) \end{aligned}$$

$$\begin{aligned} f'' + f' \left(-\frac{3}{z} + 3A_E' \right) \\ - \frac{16\pi G_5 \beta(\Phi) e^\Phi g_c^2 A_t^2 \chi^2}{f} - \frac{z^2 e^{-2A_E} A_t'^2 \mathcal{K}}{L^2} = 0, \quad (41) \end{aligned}$$

$$\begin{aligned} A_E'' - A_E' \left(-\frac{2}{z} + A_E' \right) + \frac{\phi'^2}{6} \\ + \frac{8\pi G_5 \beta(\Phi) e^\Phi g_c^2 A_t^2 \chi^2}{3f^2} + \frac{8\pi G_5 \beta(\Phi) e^\Phi \chi'^2}{3} = 0, \quad (42) \end{aligned}$$

$$\begin{aligned} \phi'' + \phi' \left(-\frac{3}{z} + \frac{f'}{f} + 3A_E' \right) - \frac{L^2 e^{2A_E}}{z^2 f} \frac{dV_\phi}{d\phi} \\ + \frac{z^2 A_t'^2}{2L^2 e^{2A_E} f} \frac{dh_\phi}{d\phi} \\ - 8\pi G_5 \left(\chi'^2 - \frac{g_c^2 A_t^2 \chi^2}{f^2} \right) \frac{d[\beta(\Phi) e^\Phi]}{d\phi} \\ - \frac{16\pi G_5 L^2 e^{2A_E}}{z^2 f} \frac{\partial \{ \beta(\Phi) e^\Phi \text{Tr} [V_X^E(\langle X \rangle, \Phi, F_E^2)] \}}{\partial \phi} \\ = 0, \quad (43) \end{aligned}$$

$$\begin{aligned} \chi'' + \chi' \left[3A_E' - \frac{3}{z} + \frac{f'}{f} + \Phi' \left(1 + \frac{1}{\beta(\Phi)} \frac{d\beta(\Phi)}{d\Phi} \right) \right] \\ + \frac{g_c^2 A_t^2 \chi}{f^2} - \frac{L^2 e^{2A_E}}{z^2 f} \frac{\partial \{ \text{Tr} [V_X^E(\langle X \rangle, \Phi, F_E^2)] \}}{\partial \chi} = 0, \quad (44) \end{aligned}$$

$$A_E'' + \frac{f''}{6f} + A_E' \left(-\frac{6}{z} + \frac{3f'}{2f} \right) - \frac{1}{z} \left(-\frac{4}{z} + \frac{3f'}{2f} \right)$$

$$\begin{aligned}
& + 3A_E'^2 - \frac{8\pi G_5 \beta(\Phi) e^\Phi g_c^2 A_t^2 \chi^2}{3f^2} \\
& + \frac{L^2 e^{2A_E} \{V_\phi + 16\pi G_5 \beta(\Phi) e^\Phi \text{Tr}[V_X^E(\langle X \rangle, \Phi, F_E^2)]\}}{3z^2 f} \\
& + \frac{32\pi G_5 \beta(\Phi) e^\Phi z^2 A_t'^2}{3L^2 e^{2A_E} f} \frac{\partial \{\text{Tr}[V_X^E(\langle X \rangle, \Phi, F_E^2)]\}}{\partial F_E^2} \\
& = 0. \tag{45}
\end{aligned}$$

UV asymptotic expansions at $z \rightarrow 0$. Near the UV boundary, the coupled equations admit fractional-

power asymptotic expansions due to the non-integer scaling dimension $\Delta_\phi = 3.8$ adopted in this work. For convenience, we list the expansions of the five background fields $\{A_t, f, A_E, \phi, \chi\}$ around $z = 0$, where the coefficients are written in terms of the canonically normalized dilaton field ϕ (recall $\phi = \sqrt{8/3} \Phi$): The coefficients involve the EMD potential parameters $\{v_0, a_4, a_6, a_8, \dots\}$ from the pure-gluon ansatz in Eq. (73) (with the best-fit set given in Eq. (76)), and the gauge-kinetic parameters $\{h_0, b_1, \dots, b_{10}\}$ from Eq. (77).

$$\begin{aligned}
A_t(z) &= c_{A_t,0} + c_{A_t,10} z^2 + \frac{5}{504} c_{A_t,10} c_{\phi,1}^2 \left(1 + \frac{42b_1^2}{1+h_0}\right) z^{\frac{12}{5}} \\
&+ \frac{5}{146821248} c_{A_t,10} c_{\phi,1}^4 \left[-8381 + \frac{5243616 b_1^4}{(1+h_0)^2} - \frac{873936}{1+h_0} (5b_1^4 - 24b_1 b_3 - 12b_2^2 h_0)\right. \\
&\quad \left. - \frac{218484 b_1^2}{1+h_0} \left(1 + 300 \left(a_4 + \frac{11}{216} v_0\right)\right) - 1820700 \left(a_4 + \frac{11}{216} v_0\right)\right] z^{\frac{14}{5}} + \mathcal{O}\left(z^{\frac{16}{5}}\right), \\
f(z) &= 1 + c_{f,20} z^4 + \frac{5}{154} c_{f,20} c_{\phi,1}^2 z^{\frac{22}{5}} + \mathcal{O}\left(z^{\frac{23}{5}}\right), \\
A_E(z) &= -\frac{1}{84} c_{\phi,1}^2 z^{\frac{2}{5}} + \frac{9}{64} c_{\phi,1}^4 \left(\frac{239}{71442} + \frac{50}{81} \left(a_4 + \frac{11}{216} v_0\right)\right) z^{\frac{4}{5}} \\
&- \frac{1}{3755372544} c_{\phi,1}^6 \left[95401 - 254016000 \left(a_6 - \frac{1019}{77760} v_0\right) + 32898600 \left(a_4 + \frac{11}{216} v_0\right)\right. \\
&\quad \left.+ 2421090000 \left(a_4 + \frac{11}{216} v_0\right)^2\right] z^{\frac{6}{5}} \\
&+ \frac{1}{36907801362432} c_{\phi,1}^8 \left[60421987 - 335428128000 \left(a_6 - \frac{1019}{77760} v_0\right) + 2300165683200 \left(a_8 + \frac{54217}{6531840} v_0\right)\right. \\
&\quad \left.- 308700 \left(-97243 + 165369600 \left(a_6 - \frac{1019}{77760} v_0\right)\right) \left(a_4 + \frac{11}{216} v_0\right)\right. \\
&\quad \left.+ 4408804890000 \left(a_4 + \frac{11}{216} v_0\right)^2\right. \\
&\quad \left.+ 184284639000000 \left(a_4 + \frac{11}{216} v_0\right)^3\right] z^{\frac{8}{5}} + \mathcal{O}(z^2), \\
\phi(z) &= c_{\phi,1} z^{\frac{1}{5}} - \frac{1}{12096} c_{\phi,1}^3 (198 + 37800 a_4 + 1925 v_0) z^{\frac{3}{5}} \\
&+ \frac{5}{12192768} c_{\phi,1}^5 \left[1734 + 40824000 a_4^2 - 6531840 a_6 + 7560 a_4 (79 + 550 v_0) + 116011 v_0 + 105875 v_0^2\right] z \\
&- \frac{1}{15021490176} c_{\phi,1}^7 \left[651899 - \frac{1579550}{27} (77760 a_6 - 1019 v_0) + 44559270000 \left(a_4 + \frac{11}{216} v_0\right)^2\right. \\
&\quad \left.- \frac{1225}{81} (-97794 + 201009600 a_6 - 2634115 v_0) (216 a_4 + 11 v_0) + \frac{160015625}{972} (216 a_4 + 11 v_0)^3\right. \\
&\quad \left.+ \frac{172480}{27} (6531840 a_8 + 54217 v_0)\right] z^{\frac{7}{5}} + \mathcal{O}\left(z^{\frac{9}{5}}\right), \\
\chi(z) &= c_{\chi,5} z + \frac{5}{6\sqrt{6}} c_{\phi,1} c_{\chi,5} \left[21 + \frac{2\beta_2}{(1+\beta_3^2)(\pi - 2 \arctan \beta_3)}\right] z^{\frac{6}{5}} \\
&+ \frac{5}{1344} c_{\phi,1}^2 c_{\chi,5} \left[8175 + \frac{1624\beta_2}{(1+\beta_3^2)(\pi - 2 \arctan \beta_3)} + \frac{42\beta_2^2}{(1+\beta_3^2)^2(\pi - 2 \arctan \beta_3)^2}\right. \\
&\quad \left.\times (-1 + 3\pi\beta_3 - 6\beta_3 \arctan \beta_3)\right] z^{\frac{7}{5}} + c_{\chi,8} z^{\frac{8}{5}} + c_{\chi,9} z^{\frac{9}{5}} + c_{\chi,10} z^2 \\
&+ c_{\chi,11} z^{\frac{11}{5}} + c_{\chi,12} z^{\frac{12}{5}} + c_{\chi,13} z^{\frac{13}{5}} + c_{\chi,14} z^{\frac{14}{5}}
\end{aligned}$$

$$+ \left[c_{\chi,15} + c_{\chi,15}^{(\log)} \ln z \right] z^3 + \mathcal{O}\left(z^{\frac{16}{5}}\right). \quad (46)$$

The UV coefficients appearing in Eq. (46) have direct boundary interpretations. For the $U(1)$ gauge field, the AdS/CFT dictionary gives the chemical potential as $\mu = A_t(z=0)$, thus

$$c_{A_t,0} = \mu. \quad (47)$$

The next coefficient $c_{A_t,10}$ is related to the baryon density rather than to μ . In the coupled system, the baryon density n_B is defined from the total Lagrangian density; see Eq. (63) in Sec. II E. Substituting the UV expansion $A_t(z) = c_{A_t,0} + c_{A_t,10}z^2 + \dots$ into Eq. (63), one can directly obtain the relation between n_B and $c_{A_t,10}$ (see the discussion below Eq. (63)).

In our numerical calculation we fix the dimensionless coefficient $c_{\phi,1}^{\text{num}} = 1$ and restore physical units by multiplying any quantity with energy dimension $[X] = E^p$ by Λ^p (see Sec. II F for our convention). In the following, we use the physical convention and simply write $c_{\phi,1} = \Lambda$ for the corresponding dimensionful UV scale, so that all UV coefficients are presented in the same physical normalization.

For the chiral scalar, the leading UV term $\chi(z) = c_{\chi,5}z + \dots$ plays the role of the source and is proportional to the (degenerate) u/d current quark mass m_u in the $N_f = 2$ setup. The coefficient of the z^3 term (together with the logarithmic piece $c_{\chi,15}^{(\log)} z^3 \ln z$) encodes the chiral condensate σ_u . It is noticed that in the present back-reacted setup the precise proportionality between $\{c_{\chi,15}, c_{\chi,15}^{(\log)}\}$ and the condensate requires holographic renormalization, because the on-shell action contains UV divergences and the prefactor $e^\Phi \beta(\Phi)$ in the Einstein-frame flavor action affects the normalization of the canonical momentum. In our numerical implementation we therefore treat $c_{\chi,5}$ as the input source parameter and use the z^3 coefficient as an indicator for the condensate; a dedicated holographic-renormalization analysis will be reported elsewhere.

It is noticed that in Eq. (46) the truly independent UV data can be chosen as $\{c_{A_t,0}, c_{A_t,10}, c_{\phi,1}, c_{\chi,5}, c_{\chi,15}\}$. All other coefficients in the UV series, such as $c_{\chi,8} - c_{\chi,14}$ and $c_{\chi,15}^{(\log)}$, are fixed by the coupled equations order by order once the above independent data and the model parameters are specified; their explicit expressions are lengthy and we do not list them here.

In practice, for a given horizon position z_h we solve the coupled boundary-value problem by fixing $c_{A_t,0}$ (set by the chemical potential μ), $c_{\chi,5}$ (set by the current quark mass m_u), and $c_{\phi,1}$ (taken as the UV scale Λ in physical units), together with the standard boundary conditions $A_t(z_h) = 0$, $f(z=0) = 1$, and $f(z_h) = 0$. The remaining conditions are provided by the UV asymptotic AdS normalizations and the regularity conditions at the horizon, which close the system for the five second-order

equations. In our numerical implementation the coupled equations are solved using a pseudospectral (collocation) method [48]. After obtaining the background solution, the temperature T (from $f'(z_h)$), the baryon density n_B (from Eq. (63)), and the chiral-condensate indicator (from the z^3 coefficient of χ) can be extracted.

In the above equations, the prime ' denotes the derivative with respect to z . Only 5 equations are independent in the above 6 equations. So we choose Eq. (45) as a constraint and use it to check the solutions of the EoMs.

Besides the second-order constraint Eq. (45), one can also derive a simplified first-order constraint equation directly from the zz component of the Einstein equations as:

$$\begin{aligned} & 4 \left(A'_E - \frac{1}{z} \right) \left(A'_E - \frac{1}{z} + \frac{f'}{4f} \right) - \frac{1}{6} \phi'^2 \\ & - \frac{8\pi G_5}{3} \beta(\Phi) e^\Phi \left(\chi'^2 + \frac{g_c^2 A_t^2 \chi^2}{f^2} \right) \\ & + \frac{L^2 e^{2A_E}}{3z^2 f} \left[V_\phi + 16\pi G_5 \beta(\Phi) e^\Phi \text{Tr}[V_X^E(\langle X \rangle, \Phi, F_E^2)] \right] \\ & + \frac{z^2 A_t'^2}{3L^2 e^{2A_E} f} \left(\frac{1}{2} h_\phi \right) \\ & + 64\pi G_5 \beta(\Phi) e^\Phi \frac{\partial \{ \text{Tr}[V_X^E(\langle X \rangle, \Phi, F_E^2)] \}}{\partial F_E^2} = 0. \end{aligned} \quad (48)$$

By using the equations of motion Eq. (41) and Eq. (42) to eliminate the second-order derivative terms f'' and A'_E in Eq. (45), one can show that it is completely equivalent to the first-order zz constraint equation Eq. (48).

In our numerical study of the back-reacted $N_f = 2$ theory, these coupled equations are solved by imposing consistency with the pure-gluon background in the limit where the flavor contribution is small.

D. Thermodynamic dictionary of the EMD system

We can get the black-hole solution from the EoMs Eq. (16)-(19). The temperature of the black-hole is

$$T = \left| \frac{f'(z_h)}{4\pi} \right|, \quad (49)$$

where z_h is the location of the horizon for the black-hole. The entropy density of the black-hole is

$$s_{EMD} = \frac{e^{3A_E(z_h)}}{\frac{\kappa_5^2}{2\pi} z_h}. \quad (50)$$

According to the AdS/CFT dictionary, the temperature and the entropy density of the QCD matter are T and s_{EMD} , respectively.

According to the AdS/CFT dictionary, the chemical potential is

$$\mu = A_t(z=0), \quad (51)$$

and the baryon number density is

$$\begin{aligned} n_{EMD} &= \left| \lim_{z \rightarrow 0} \frac{\partial \mathcal{L}^E}{\partial (\partial_z A_t)} \right| \\ &= -\frac{1}{2\kappa_5^2} \lim_{z \rightarrow 0} \left[\frac{e^{A_E(z)}}{z} h_\phi(\phi) \frac{d}{dz} A_t(z) \right], \end{aligned} \quad (52)$$

where \mathcal{L}^E is the Lagrangian density in the Einstein frame in Eq. (10). From the Euler-Lagrange equation of the field $A_t(z)$:

$$\partial_M \frac{\partial \mathcal{L}^E}{\partial (\partial_M A_t)} - \frac{\partial \mathcal{L}^E}{\partial A_t} = 0, \quad (53)$$

$$\partial_z \left[\frac{e^{A_E(z)}}{z} h_\phi(\phi) \frac{d}{dz} A_t(z) \right] = 0. \quad (54)$$

Eq. (54) is actually the EoM of A_t Eq. (16). Thus, we get the conserved Gauss charge associated with the field A_t :

$$Q_G = \frac{e^{A_E(z)}}{z} h_\phi(\phi) \frac{d}{dz} A_t(z). \quad (55)$$

Then we derive

$$n_{EMD} = -\frac{1}{2\kappa_5^2} Q_G. \quad (56)$$

Sometimes the following expression of n_{EMD} which is related to the quantities at the black-hole horizon is more convenient in the calculation:

$$n_{EMD} = -\frac{1}{2\kappa_5^2} \frac{e^{A_E(z_h)}}{z_h} h_\phi(\phi = \phi(z_h)) A_t'(z_h). \quad (57)$$

The internal energy density and the free energy density are

$$\begin{aligned} \epsilon_{EMD} &= T s_{EMD} - p_{EMD} + \mu n_{EMD}, \\ \mathcal{F}_{EMD} &= -p_{EMD} = \epsilon_{EMD} - T s_{EMD} - \mu n_{EMD}. \end{aligned} \quad (58)$$

The differential relation of the above equations are

$$\begin{aligned} d\epsilon_{EMD} &= T ds_{EMD} + \mu dn_{EMD}, \\ d\mathcal{F}_{EMD} &= -dp_{EMD} = -s_{EMD} dT - n_{EMD} d\mu. \end{aligned} \quad (59)$$

From Eq. (59), we can calculate the pressure P and the internal energy density ϵ . The trace anomaly is

$$\begin{aligned} I_{EMD}(T, \mu) &= \epsilon_{EMD}(T, \mu) - 3p_{EMD}(T, \mu) \\ &= T s_{EMD}(T, \mu) + \mu n_{EMD}(T, \mu) \end{aligned}$$

$$-4p_{EMD}(T, \mu). \quad (60)$$

The square of the speed of sound is

$$c_{sEMD}^2 = \frac{dp_{EMD}}{d\epsilon_{EMD}}. \quad (61)$$

The adiabatic index γ is

$$\gamma = \frac{d \ln p_{EMD}}{d \ln \epsilon_{EMD}}. \quad (62)$$

Here all the thermodynamic quantities are labeled with ‘‘EMD’’, which means these thermodynamic quantities are determined by the EMD system.

E. Thermodynamic dictionary of the coupled EMD+KKSS system

We now briefly comment on the thermodynamic dictionary for the coupled system $S_{\text{total}}^E = S_{EMD}^E + S_f^E$. The thermodynamics is still determined by the black-hole background geometry: the temperature is given by Eq. (49), and the entropy density is given by the Bekenstein–Hawking area formula, which takes the same form as Eq. (50) but with the back-reacted metric function $A_E(z)$ obtained from the coupled equations. The chemical potential is still identified as the boundary value $\mu = A_t(z=0)$, i.e. Eq. (51).

The main difference from the pure EMD case is the baryon number density. In the coupled system it should be defined from the total Lagrangian density,

$$\begin{aligned} n_B &= \left| \lim_{z \rightarrow 0} \frac{\partial \mathcal{L}_{\text{total}}^E}{\partial (\partial_z A_t)} \right| \\ &= -\frac{1}{2\kappa_5^2} \lim_{z \rightarrow 0} \left[\frac{e^{A_E(z)}}{z} \mathcal{K}(z) \frac{d}{dz} A_t(z) \right], \end{aligned} \quad (63)$$

where $\mathcal{L}_{\text{total}}^E$ denotes the Lagrangian density corresponding to S_{total}^E , and $\mathcal{K}(z)$ is the effective gauge kinetic function defined in Eq. (39). Using the UV expansion $A_t(z) = \mu + c_{A_t,10} z^2 + \dots$ together with $A_E(0) = 0$ and $\beta(\Phi \rightarrow 0) \rightarrow 0$ (thus $\mathcal{K}(0) = h_\phi(0) = 1$), one finds

$$n_B = -\frac{\mathcal{K}(0)}{8\pi G_5} c_{A_t,10} = -\frac{1}{8\pi G_5} c_{A_t,10}, \quad (64)$$

where we used $\kappa_5^2 = 8\pi G_5$. It is noticed that the Euler–Lagrange equation for A_t no longer reduces to a conservation law when the flavor sector is coupled: the Maxwell equation contains source terms (see Eq. (40) in the general case), thus the Gauss charge Q_G is not conserved and Eqs. (54)–(57) do not apply to the coupled system.

Other thermodynamic relations keep the same form, e.g. $\epsilon = Ts - P + \mu n$ and $dP = s dT + n d\mu$, with (s, n) understood as the entropy and baryon density of the coupled system.

F. Model input and our working conventions

In this work, we use the same EMD+KKSS framework but focus on two distinct approximations/interpretations. Firstly, in the probe approximation we solve the EMD equations of motion and interpret the background as an effective description of $(2+1)$ -flavor QCD matter. Secondly, we go beyond the probe approximation and solve the coupled EMD+KKSS equations with back-reaction; in this step we use the pure-gluon lattice EoS to fix the EMD sector, and then interpret the back-reacted solution as the $N_f = 2$ theory.

The main model inputs are the dilaton potential and the gauge kinetic function in the EMD sector, $V_\phi(\phi)$ and $h_\phi(\phi)$, together with the KKSS couplings $\beta(\Phi)$ and V_X . In our Mathematica code, we used a convention in which many variables carry a prefix “var”; in this paper we always drop that prefix and use the standard symbols.

The (pure) EMD system admits an overall scaling symmetry: after setting the AdS radius to unity one first obtains thermodynamic quantities in “bulk units”, and then introduces a single characteristic energy scale Λ to convert them to physical units, following the convention in Ref. [14]. Any quantity X with energy dimension $[X] = E^p$ is mapped as

$$X_{\text{phys}} = \Lambda^p X_{\text{bulk}}. \quad (65)$$

In particular, $T = \Lambda T_{\text{bulk}}$, $\mu_B = \Lambda (\mu_B)_{\text{bulk}}$, $s = \Lambda^3 s_{\text{bulk}}$, $n_B = \Lambda^3 (n_B)_{\text{bulk}}$, and $P, \epsilon = \Lambda^4 (P, \epsilon)_{\text{bulk}}$. Therefore, dimensionless combinations such as s/T^3 and P/T^4 do not depend on Λ . Equivalently, Λ may be viewed as a conversion factor between the (dimensionless) coordinate/field normalization adopted in the bulk and the physical normalization used to report results in MeV/GeV. This freedom is a direct consequence of the overall scale invariance of the classical EMD equations (after fixing the AdS radius $L = 1$): a simultaneous rescaling of boundary coordinates and intensive thermodynamic quantities leaves all dimensionless observables invariant, while it changes the numerical values of dimensionful quantities by a common factor. In practice, once a specific calibration prescription at $\mu = 0$ is chosen (e.g. matching the lattice curve of $s(T)/T^3$ or fixing a reference temperature in physical units), Λ is fixed and does not represent an additional tunable parameter. Throughout this paper, we use Λ to denote this overall scale (not to be confused with other uses of Λ in unrelated contexts).

III. PROBE APPROXIMATION: EMD CALIBRATED TO THE LATTICE EOS OF $(2+1)$ FLAVORS VIA NEURAL ODE

In this section, we work in the probe approximation: we neglect the back-reaction of the KKSS flavor sector and only solve the EMD equations of motion given in Sec. II. After obtaining the black hole backgrounds, we calculate

the thermodynamic quantities and compare the resulting equation of state with the lattice QCD EoS for $(2+1)$ flavors at finite temperature and finite baryon chemical potential.

A. Neural-ODE calibration strategy

In this part, we calibrate the EMD model to the lattice EoS using neural ODE framework [29, 30]. The EMD equations are treated as a differentiable ODE system, and the model functions $V_\phi(\phi)$ and $h_\phi(\phi)$ are learned from data under UV/IR constraints. The parameters are optimized by minimizing the mismatch between the holographic predictions and the lattice targets.

Once $V_\phi(\phi)$ and $h_\phi(\phi)$ are determined, we keep them fixed and use the same five-dimensional action for all black-hole solutions at different (T, μ_B) . This keeps the thermodynamic state dependence in the solutions rather than in temperature-dependent effective potentials, and makes the subsequent back-reaction study a direct probe of the limitations of the coupled ansatz.

In this probe calibration, we use as reference a recently published thermodynamic table for $(2+1)$ -flavor QCD at finite temperature and finite baryon chemical potential, with $\mu_Q = \mu_S = 0$ and $T = 35.0$ – 490.0 MeV [49]. This table is released through a public interpolation/fitting framework that combines lattice-QCD constraints with a hadron-resonance-gas (HRG) description [50], and provides a broad and smooth domain that is convenient for a stable inverse reconstruction of the model functions. Our conventions for the EMD background and thermodynamic extraction follow standard choices in the recent holographic EMD literature; see, e.g., Ref. [15]. In our training set we include the dimensionless ratio s/T^3 (and thus also p/T^4 , ϵ/T^4 and $I/T^4 \equiv (\epsilon - 3p)/T^4$ derived from thermodynamic identities) at $\mu = 0$, together with s/T^3 and n_B/T^3 at finite μ .

To reduce degeneracies in the inverse fit, we build the model functions by combining hard UV/IR constraints with a flexible data-driven component. Specifically, we impose the UV behavior $V_\phi(\phi) = -12 + \frac{1}{2}m_\phi^2\phi^2 + \mathcal{O}(\phi^4)$ and $h_\phi(\phi) = 1 + \mathcal{O}(\phi)$ at $\phi \rightarrow 0$. The UV mass term is fixed by the scaling dimension Δ_ϕ through the AdS/CFT relation in Eq. (11); see also the discussion in Sec. II. In the IR we include a term that enforces asymptotically linear glueball spectra, and set $\Delta_\phi = 3.6$ (thus $\nu = 4 - \Delta_\phi = 0.4$ and $m_\phi^2 = \Delta_\phi(\Delta_\phi - 4)$) together with a fixed IR coefficient $k_V = -0.1$. The remaining parts of $V_\phi(\phi)$ and $h_\phi(\phi)$ are then learned from data in the neural-ODE optimization. In practice, the flexible components are represented by fully connected neural networks with a simple 1–24–24–1 architecture and SiLU activation.

For later use, we provide an explicit functional parametrization for the reconstructed model functions. In our convention, the Einstein-frame gluon potential and

the gauge kinetic function are taken as

$$\begin{aligned}
V_\phi(\phi) = & -12 + \frac{1}{2}m_\phi^2\phi^2 + V_{\text{net}}(\phi)\phi^4 \\
& + k_V(1 + \phi^2)^{\frac{1}{4}} \exp\left(\frac{\sqrt{6}}{3}\phi\right) \\
& - \left[k_V + k_V \frac{\sqrt{6}}{3}\phi + \frac{7}{12}k_V\phi^2 \right. \\
& \quad \left. + \frac{13}{36}k_V \frac{\sqrt{6}}{3}\phi^3 + \frac{5}{288}k_V\phi^4 \right], \quad (66)
\end{aligned}$$

and

$$\begin{aligned}
h_\phi(\phi) = & k_{h_1} \exp(k_{h_2}\phi) \\
& + (1 - k_{h_1}) \exp[-\phi h_{\text{net}}(\phi)], \quad (67)
\end{aligned}$$

where $V_{\text{net}}(\phi)$ and $h_{\text{net}}(\phi)$ denote the flexible components represented by neural networks. The subtraction terms in Eq. (66) ensure that the UV expansion matches $V_\phi(\phi) = -12 + \frac{1}{2}m_\phi^2\phi^2 + \mathcal{O}(\phi^4)$ while keeping the desired IR asymptotics.

For later reference, we fit the trained network outputs by simple polynomials (valid in the data-constrained range of ϕ shown in Fig. 4):

$$\begin{aligned}
V_{\text{net}}(\phi) = & -1.558082 \times 10^{-7}\phi^8 \\
& + 4.058989 \times 10^{-6}\phi^7 \\
& - 2.014347 \times 10^{-5}\phi^6 \\
& - 3.300564 \times 10^{-4}\phi^5 \\
& + 4.517985 \times 10^{-3}\phi^4 \\
& - 2.073986 \times 10^{-2}\phi^3 \\
& + 3.797004 \times 10^{-2}\phi^2 \\
& + 6.484887 \times 10^{-4}\phi \\
& - 1.702365 \times 10^{-1}, \quad (68)
\end{aligned}$$

$$\begin{aligned}
h_{\text{net}}(\phi) = & 7.523421 \times 10^{-7}\phi^8 \\
& - 3.743422 \times 10^{-5}\phi^7 \\
& + 7.309245 \times 10^{-4}\phi^6 \\
& - 6.995335 \times 10^{-3}\phi^5 \\
& + 3.262371 \times 10^{-2}\phi^4 \\
& - 6.210014 \times 10^{-2}\phi^3 \\
& + 9.327736 \times 10^{-2}\phi^2 \\
& - 1.261251 \times 10^{-1}\phi \\
& + 8.025826 \times 10^{-2}. \quad (69)
\end{aligned}$$

The best-fit constants in Eqs. (66)–(67) are

$$\begin{aligned}
\Delta_\phi = 3.6, & & \nu = 4 - \Delta_\phi = 0.4, \\
m_\phi^2 = \Delta_\phi(\Delta_\phi - 4) = -1.44, & & k_V = -0.1, \\
k_{h_1} = 0.652974, & & k_{h_2} = -11.292836,
\end{aligned}$$

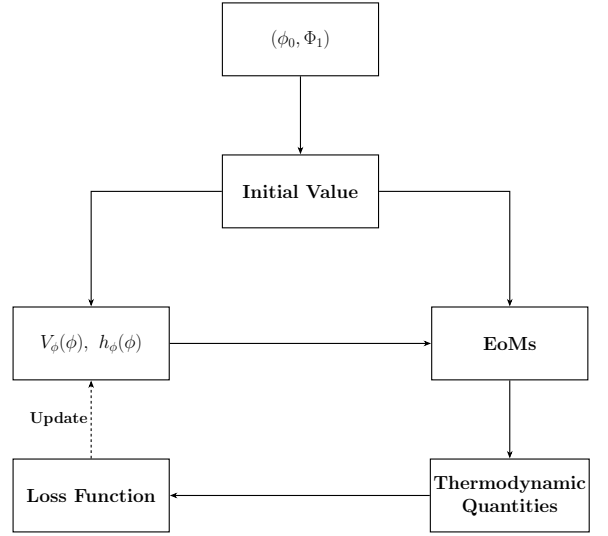


FIG. 1. Schematic illustration of the neural-ODE calibration workflow. For a given set of model-function parameters, the EMD equations are solved to obtain thermodynamic observables, which are compared with the reference table to construct the loss, and the parameters are updated by gradient-based optimization.

$$\Lambda = 1130.97 \text{ MeV}, \quad \kappa_5^2 = 10.39. \quad (70)$$

In this probe calibration we take $\Delta_\phi = 3.6$, while in the pure-gluon/back-reacted steps below we adopt a different value (e.g. $\Delta_\phi = 3.8$) tailored to that calibration; we keep the same notation to match the corresponding numerical setups.

The training is performed in two stages. First, we fix $\mu = 0$ and optimize $V_\phi(\phi)$ by matching s/T^3 . Second, we freeze the trained $V_\phi(\phi)$ and optimize $h_\phi(\phi)$ by matching both s/T^3 and n_B/T^3 at finite μ . For a data sample at (T_i, μ_i) with uncertainty e_i , we define the loss functions as

$$L_{s/T^3} = \frac{1}{N} \sum_i \left[\frac{(s/T^3)_{m_i} - (s/T^3)_{d_i}}{(s/T^3)_{e_i}} \right]^2, \quad (71)$$

$$\begin{aligned}
L_{n_B/T^3} = & \frac{1}{N} \sum_i \left[\left(\ln(n_B/T^3)_{m_i} - \ln(n_B/T^3)_{d_i} \right) \right. \\
& \left. \times \frac{(n_B/T^3)_{d_i}}{(n_B/T^3)_{e_i}} \right]^2, \quad (72)
\end{aligned}$$

where the subscripts m_i , d_i , and e_i denote the model prediction, the reference-data value, and the data uncertainty, respectively. The logarithmic form in Eq. (72) balances the wide dynamic range of n_B/T^3 . We propagate gradients through the differentiable EMD solver using an adjoint sensitivity method [29, 30] to efficiently optimize the network parameters.

B. EoS results and comparison with lattice

After training, we obtain an excellent agreement with the reference thermodynamic table for $(2+1)$ -flavor QCD in a wide range of temperature and chemical potential. In Fig. 2 we show representative comparisons at $\mu = 0$, while in Fig. 3 we show the comparisons in fixed μ/T slices in the temperature window $T = 35\text{--}490$ MeV.

As an additional application of the reconstructed probe-approximation model, one may explore the thermodynamics at finite μ and infer the possible location of the critical endpoint (CEP). Following the standard procedure, we inspect the behavior of $T(s, \mu_B)$ and identify the CEP from the extremum of dT/ds along fixed- μ_B curves. An illustration of this determination is shown in Fig. 5. With this procedure, the CEP in the present reconstructed probe model is located at approximately $(T^{\text{CEP}}, \mu_B^{\text{CEP}}) \approx (89.4 \pm 0.2, 630.5 \pm 1.0)$ MeV.

IV. PURE-GLUE CALIBRATION OF THE EMD SECTOR AT $\mu = 0$

We now consider the EMD system as a dual description of the pure Yang–Mills theory. In this step we set $\mu_B = 0$, thus $A_t(z) = 0$, and the Maxwell sector decouples. Therefore the gauge kinetic function $h_\phi(\phi)$ does not enter the thermodynamics at $\mu_B = 0$, and the pure-gluon calibration mainly constrains the dilaton potential $V_\phi(\phi)$ and the overall normalizations.

A. Ansatz for $V_\phi(\phi)$ and fitted parameters

We take the following analytic ansatz in $d = 4$:

$$\begin{aligned} V_\phi(\phi) = & -d(d-1) \\ & + \left[\frac{\Delta_\phi(\Delta_\phi - d)}{2} - \frac{v_0}{2(d-1)} \right] \phi^2 \\ & + a_4\phi^4 + a_6\phi^6 + a_8\phi^8 + a_{10}\phi^{10} \\ & + v_0(1 + \phi^2)^{\frac{1}{4}} \left[\sinh\left(\frac{\phi}{\sqrt{2(d-1)}}\right) \right]^2, \end{aligned} \quad (73)$$

which is UV consistent by construction.

Indeed, expanding Eq. (73) around $\phi = 0$ one finds

$$\begin{aligned} & v_0(1 + \phi^2)^{\frac{1}{4}} \left[\sinh\left(\frac{\phi}{\sqrt{2(d-1)}}\right) \right]^2 \\ & = \frac{v_0}{2(d-1)} \phi^2 + \mathcal{O}(\phi^4), \end{aligned} \quad (74)$$

which cancels the explicit $-\frac{v_0}{2(d-1)}\phi^2$ term in the second line. Therefore the quadratic coefficient is fixed to be $\frac{\Delta_\phi(\Delta_\phi - d)}{2}$, in agreement with the AdS/CFT mass-dimension relation. In particular, for $d = 4$ one has

$m_\phi^2 L^2 = \Delta_\phi(\Delta_\phi - 4)$, see Eq. (11); in our numerical implementation we set $L = 1$ as discussed around Eq. (3). This structure ensures that the background is asymptotically AdS and that the UV scaling dimension Δ_ϕ of the operator dual to ϕ is well-defined, while still allowing v_0 to control the nonconformal/IR behavior without spoiling the UV data. In the present fit we take $\Delta_\phi = 3.8$.

The best-fit parameters obtained by a hybrid optimization (Bayesian optimization combined with local refinement) are

$$\begin{aligned} \Lambda &= 1.19785 \text{ GeV}, \\ G_5 &= 1.16750, \end{aligned} \quad (75)$$

and

$$\begin{aligned} v_0 &= -\frac{6}{5}, \\ a_4 &= -7.74146 \times 10^{-2}, \\ a_6 &= -3.48325 \times 10^{-4}, \\ a_8 &= -1.36440 \times 10^{-5}, \\ a_{10} &= -2.89020 \times 10^{-8}. \end{aligned} \quad (76)$$

Here Λ is the overall energy scale of the EMD system introduced to convert bulk units to physical units; see Eq. (65) and Ref. [14].

B. A convenient ansatz for $h_\phi(\phi)$

For use at finite μ , we also record the functional form of the gauge kinetic function $h_\phi(\phi)$:

$$\begin{aligned} h_\phi(\phi) = & \frac{1}{1 + h_0} \text{sech}(b_1\phi + b_3\phi^3 + b_5\phi^5 \\ & + b_7\phi^7 + b_9\phi^9) \\ & + \frac{h_0}{1 + h_0} \text{sech}(b_2\phi^2 + b_4\phi^4 + b_6\phi^6 \\ & + b_8\phi^8 + b_{10}\phi^{10}), \end{aligned} \quad (77)$$

where the set of parameters $\{h_0, b_1, \dots, b_9, b_2, \dots, b_{10}\}$ are to be fixed.

It is noticed again that at $\mu = 0$ the Maxwell sector decouples and $h_\phi(\phi)$ does not enter the thermodynamics.

C. Pure-gluon EoS at $\mu = 0$

In practice, the pure-gluon calibration amounts to minimizing a chi-square objective constructed from the lattice entropy density s/T^3 at $\mu = 0$. Concretely, for each lattice temperature point T_i (with uncertainty σ_i), we define

$$\chi^2 = \sum_{i \geq 6} \left[\frac{\left(\frac{s}{T^3}\right)_{\text{model}}|_{T=T_i} - \left(\frac{s}{T^3}\right)_{\text{lat}}|_{T=T_i}}{\sigma_i} \right]^2, \quad (78)$$

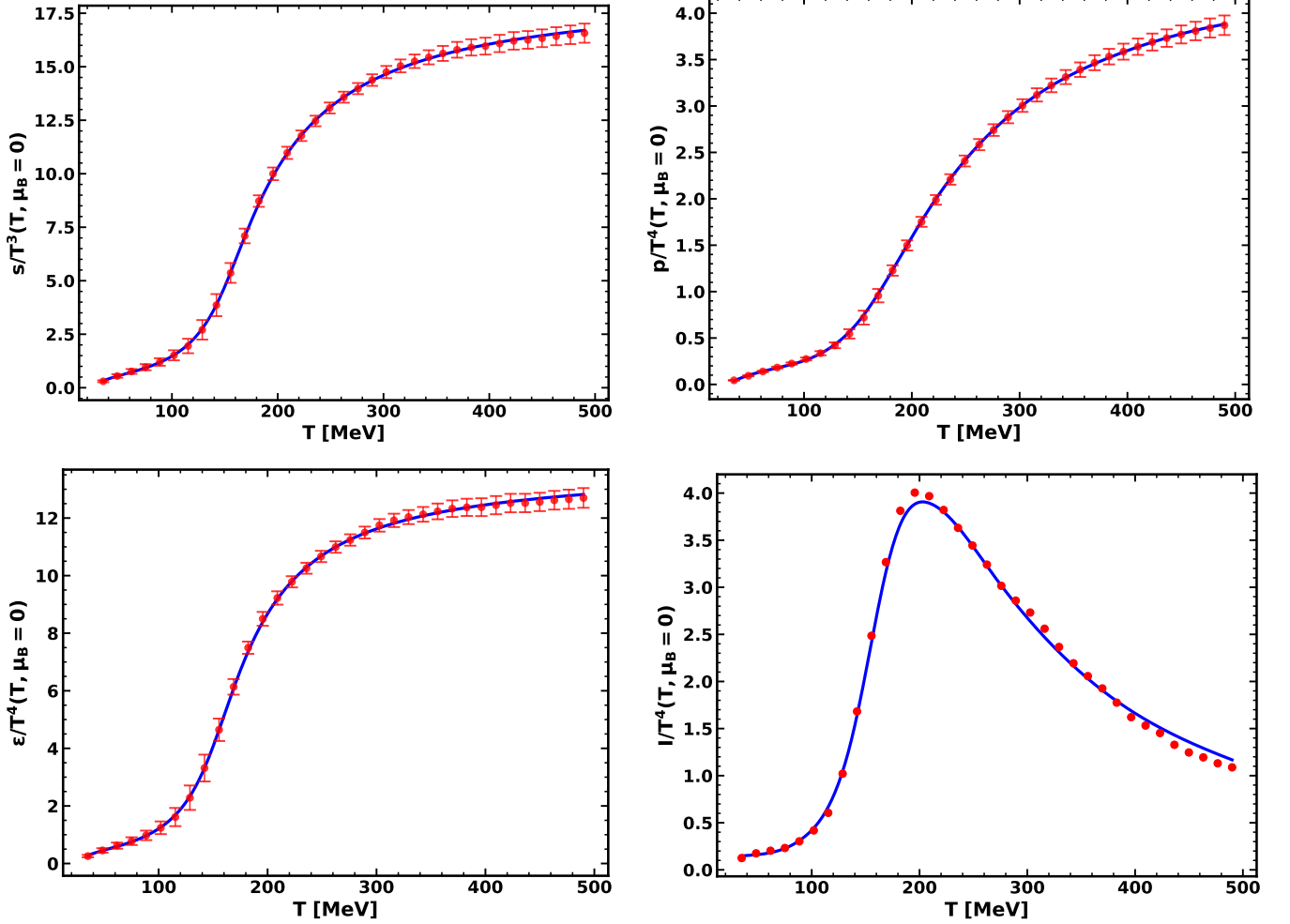


FIG. 2. Probe approximation, $(2 + 1)$ flavors at $\mu = 0$: comparison between the holographic EMD results (solid lines) and the reference thermodynamic table [49] (scatter points). Upper left panel: s/T^3 ; upper right panel: p/T^4 ; lower left panel: ϵ/T^4 ; lower right panel: $I/T^4 = (\epsilon - 3p)/T^4$. The reference points for I/T^4 are constructed from the combination $\epsilon - 3p$ and thus do not represent an independently tabulated observable. The horizontal axis is T in units of MeV.

and determine the best-fit model parameters by minimizing χ^2 . In practice, the sum starts from the 6th lattice temperature point (excluding the five points below T_c), because their absolute uncertainties are very small and would otherwise over-weight the near-transition region in the chi-square objective. Since each function evaluation requires solving the background and extracting thermodynamic quantities, we adopt a hybrid Bayesian-optimization strategy based on a Gaussian-process surrogate model [51–53], combined with local refinement. Starting from an initial Latin-hypercube sampling in the parameter box, we iteratively fit the surrogate to the accumulated samples, propose new candidates by alternating a local acquisition-based search around the current best point (with an adaptive search radius) and occasional global exploration, and evaluate the expensive objective in parallel; failed evaluations are discarded and successful samples are cached to enable restartable runs.

With the best-fit parameter set, we compute the EoS at $\mu = 0$ and compare it with the lattice Yang–Mills result, as shown in Fig. 6. The red points are the lattice $SU(3)$ data from Ref. [54].

V. COUPLED EMD+KKSS SYSTEM WITH BACK-REACTION AND THE $N_f = 2$ EOS

In this section, we go beyond the probe approximation and solve the coupled EMD+KKSS equations with back-reaction. The logic is the following:

- we first fix the EMD sector by fitting the pure-gluon lattice EoS at $\mu = 0$, as shown in Sec. IV;
- then we turn on the KKSS sector and solve the coupled equations, and interpret the back-reacted solution as a dual description of the $N_f = 2$ theory.

A. Coupled equations and numerical setup

From the numerical point of view, turning on the flavor back-reaction turns the thermodynamic problem into a genuinely coupled boundary-value system: one has to solve five second-order ODEs for $\{A_E(z), f(z), \phi(z), A_t(z), \chi(z)\}$ subject to UV AdS normalizations and horizon regularity conditions, and the solution determines (T, n_B, σ_u) simultaneously. This coupled structure (together with the fractional-power UV asymptotics induced by $\Delta_\phi = 3.8$) makes the back-reacted step substantially more constrained and more delicate than the probe calculation, and it also provides a clean arena to diagnose which model ingredients are still missing.

Varying the total action in Eq. (1) gives a coupled system of equations for $\{A_E(z), f(z), \phi(z), A_t(z), \chi(z)\}$. In the present back-reaction study we focus on the thermodynamic sector and keep the dominant χ

contribution in the KKSS action, while the meson and baryon excitations are neglected, as explained in Sec. II B. The χ equation of motion is given in Eq. (44), and the back-reaction enters through the modified Einstein equations, where the energy-momentum tensor receives additional contributions from the flavor sector.

For completeness, we keep the general form of the coupled equations below. However, in the EoS comparison reported in this section we work at $\mu = 0$ and finite temperature, thus $A_t(z) \equiv 0$ and the Maxwell sector decouples.

The numerical integration is performed by imposing UV regularity and horizon regularity, and one of the Einstein equations is used as a constraint to check the solutions.

More explicitly, we adopt the standard black hole ansatz in the Einstein frame, Eq. (12), with horizon located at $z = z_h$ where $f(z_h) = 0$. The Hawking temperature is obtained from Eq. (49). At the UV boundary $z \rightarrow 0$, we impose the asymptotic AdS behavior and the UV expansions summarized in Eq. (46). At the horizon, all fields are required to be regular, which fixes the near-horizon expansions and reduces the number of free shooting parameters.

It is noticed that the coupled system contains redundant equations due to diffeomorphism invariance. In practice, we solve a convenient subset of the coupled equations and use one Einstein equation as a constraint (analogous to the role of Eq. (20) in the probe EMD system) to monitor the numerical accuracy of the solution.

B. KKSS input: $\beta(\Phi)$ and V_X

The KKSS sector is specified by the function $\beta(\Phi)$ and the scalar potential $V_X^s(X; \Phi, F^2)$ (or equivalently its Einstein-frame form V_X^E). In the $N_f = 2$ case, the bulk scalar X is a 2×2 matrix. In the thermodynamic sector considered here we take its vacuum expectation value in the diagonal form $\langle X \rangle = \frac{\chi(z)}{2} I_2$, thus only $\text{Tr} V_X$ enters. In the coupled $N_f = 2$ calculation reported here, we fix the KKSS polynomial potential parameters $\lambda_2 = -3$ and $\lambda_4 = 168/5$ (see Eq. (23) and the discussion in Sec. II B), and set the covariant-derivative coupling $g_c = 0$. For the flavor-backreaction strength we adopt the smooth ansatz in Eq. (25) with $\beta_2 = 1$ and $\beta_3 = 50$, while β_1 is varied to perform a comparison study:

$$\begin{aligned} \beta_1 &\in \{21, 23, 25\}, \\ \beta_2 &= 1, \\ \beta_3 &= 50, \\ g_c &= 0, \\ \lambda_4 &= \frac{168}{5}, \\ m_u &= 24.826 \text{ MeV}, \end{aligned} \tag{79}$$

where β_1 controls the overall magnitude of $\beta(\Phi)$ and thus the strength of the flavor back-reaction; the three values

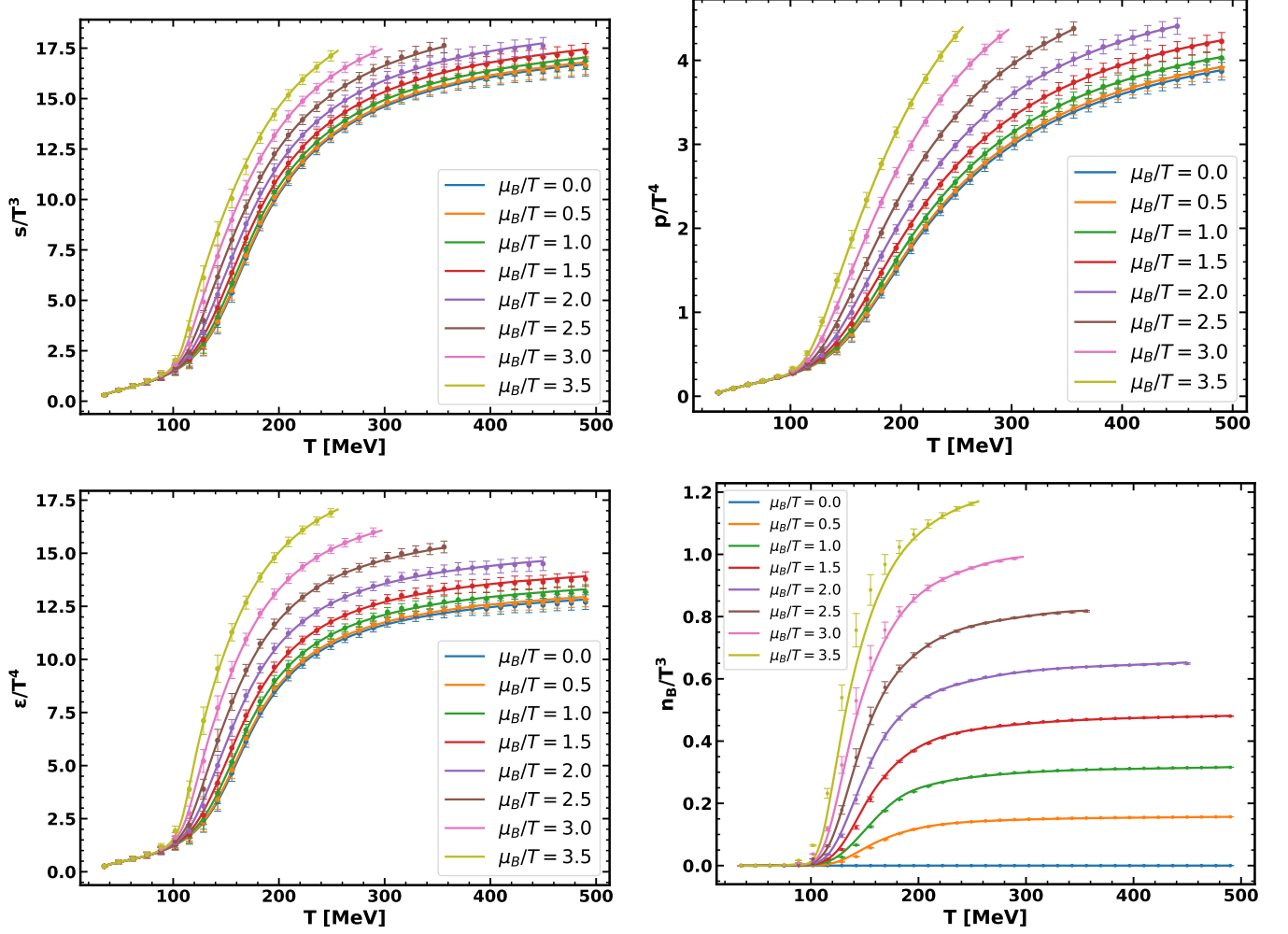


FIG. 3. Probe approximation, (2 + 1) flavors in fixed μ/T slices (temperature window $T = 35\text{--}490$ MeV): comparisons between the holographic EMD results (solid lines) and the reference thermodynamic table [49] (scatter points). Upper left panel: s/T^3 ; upper right panel: p/T^4 ; lower left panel: ϵ/T^4 ; lower right panel: n_B/T^3 .

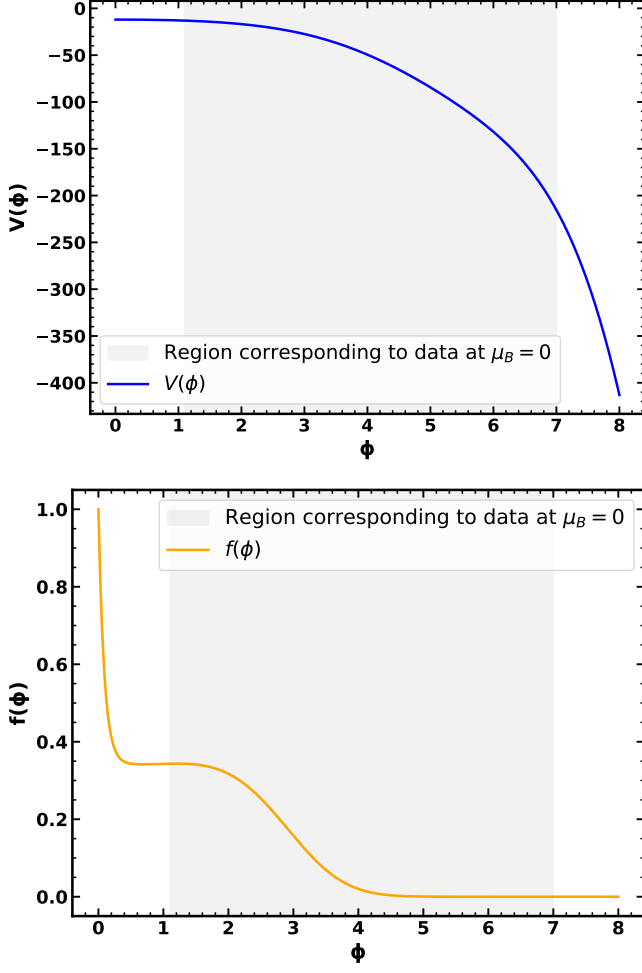


FIG. 4. Probe calibration via neural ODE: reconstructed model functions $V_\phi(\phi)$ (upper panel) and $h_\phi(\phi)$ (lower panel). The shaded region indicates the range of ϕ values effectively covered by the input thermodynamic data at $\mu = 0$ (in the present dataset, roughly $\phi \simeq 1.1\text{--}7.0$), which provides a practical measure of the domain where the reconstruction is best constrained.

above are used to assess the corresponding systematic uncertainty in the $N_f = 2$ EoS comparison.

Ref. [55] reported the $N_f = 2$ lattice EoS for three sets of bare parameters (corresponding to different pion masses), and in this work we compare with their $m_\pi = 360$ MeV ensemble. Accordingly, the input light-quark mass in our holographic calculation is not taken at the physical point. Since the present thermodynamic truncation does not compute the pion mass directly, we fix the degenerate u/d current quark mass m_u using the Gell-Mann–Oakes–Renner relation, i.e. $m_u \propto m_\pi^2$ at fixed f_π and condensate normalization, and rescale from the physical pion mass. This gives $m_u = 24.826$ MeV, which is used as the source parameter $c_{\chi,5}$ in the coupled $N_f = 2$ study reported below.

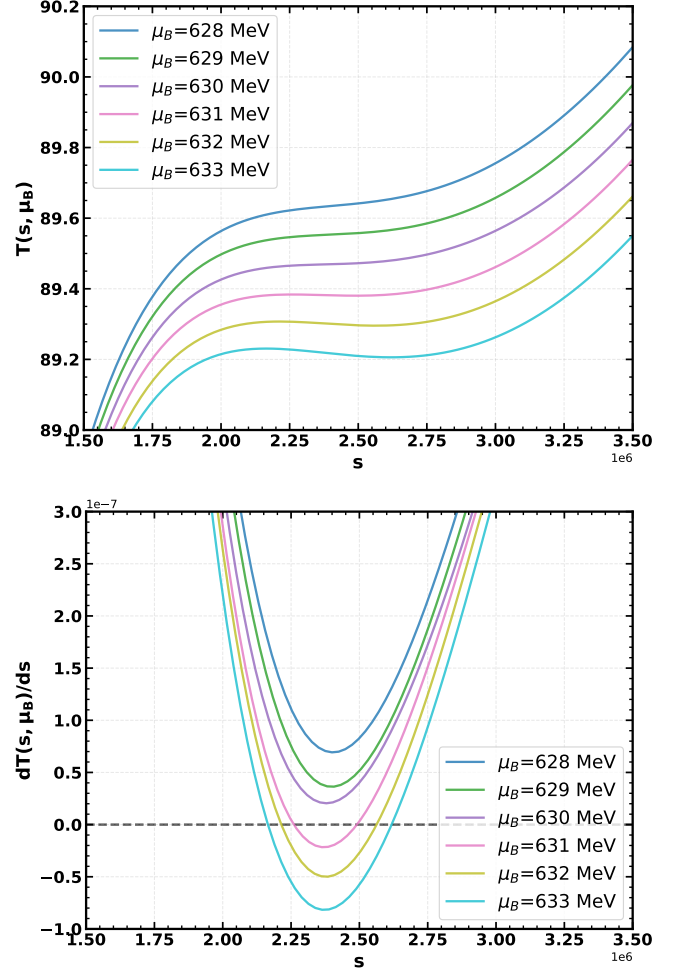


FIG. 5. Determination of the QCD critical endpoint (CEP) in the probe-approximation model. Upper panel: $T(s, \mu_B)$ curve with the CEP marked by a red dot. Lower panel: dT/ds curve, where the extremum (black star) corresponds to the CEP.

C. Two-flavor EoS and comparison with lattice

With the EMD parameters fixed by the pure-gluon calibration, we solve the coupled system and compute the EoS at $\mu = 0$. We then compare the result with the lattice EoS of $N_f = 2$ QCD. We find that a visible mismatch remains: by manually tuning the KKSS parameters one can reproduce the overall trend, but quantitative differences persist in some temperature ranges. We also tried a hybrid optimization strategy for the KKSS parameters, but the improvement is limited and the fit quality is still not satisfactory. This mismatch may indicate limitations of the current ansatz for $\beta(\Phi)$ and/or V_X in the present truncation of the flavor sector. In particular, as will be seen from the high-temperature behavior below, the coupled results tend to a nearly β_1 -insensitive plateau close to the $\beta_1 = 0$ (pure-gluon) curve, suggesting that the present KKSS truncation may not provide sufficient high- T flavor contribution in the

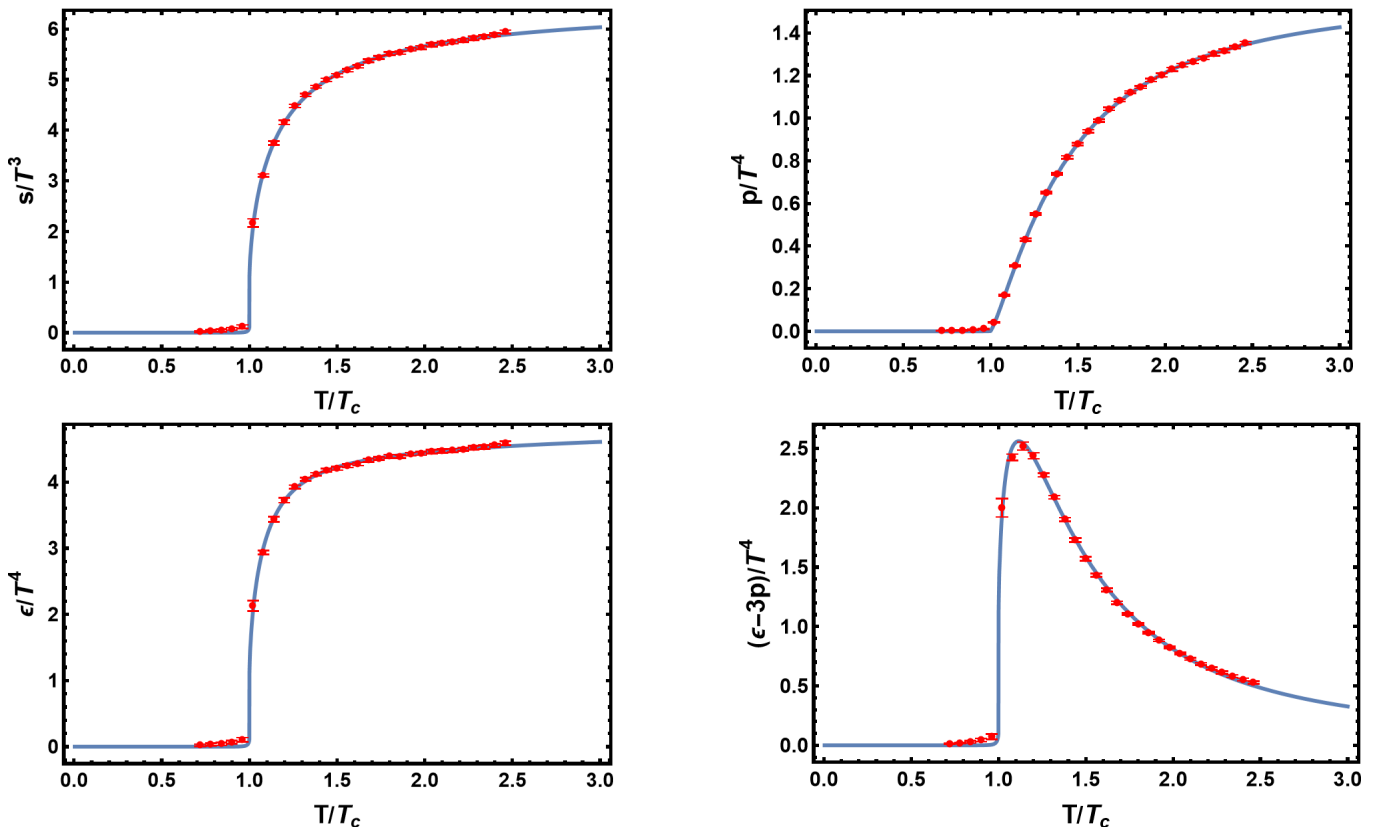


FIG. 6. Pure-gluon calibration of the EMD sector at $\mu = 0$: comparison between the holographic EoS and the lattice Yang–Mills EoS [54]. Upper left panel: the ratio of entropy density over cubic temperature, s/T^3 . Upper right panel: the ratio of pressure over quartic temperature, p/T^4 . Lower left panel: the ratio of internal energy density over quartic temperature, ϵ/T^4 . Lower right panel: the trace anomaly over quartic temperature, $I/T^4 = (\epsilon - 3p)/T^4$. In all panels the horizontal axis is the scaled temperature T/T_c . The blue solid lines are our holographic results. The red points (with error bars) are the lattice data from Ref. [54].

thermodynamics.

1. Sensitivity to the back-reaction strength parameter β_1

In Fig. 7, we compare the back-reacted holographic result for $3p/T^4$ with the $N_f = 2$ lattice band of Ref. [55], for three representative values $\beta_1 = 21, 23, 25$. We find that the holographic EoS captures the overall trend of the lattice result, but it is not completely inside the lattice uncertainty band in the full temperature window. More concretely, increasing β_1 raises the holographic curve. This improves the agreement at higher temperatures, but it can also spoil the agreement at lower temperatures: for $\beta_1 = 21$ the low- T region is closer to the lattice band while the high- T region tends to undershoot, whereas for $\beta_1 = 25$ the curve is lifted and becomes closer to the band at higher T at the price of overshooting at lower T .

The origin of this behavior can be traced back to the role of β_1 in the KKSS sector. The function $\beta(\Phi)$ in Eq. (21) controls the coupling strength between the flavor sector and the EMD background. With the smooth ansatz in Eq. (25), $\beta(\Phi)$ interpolates from 0 in the UV to β_1

in the IR, so β_1 sets the overall magnitude of the flavor back-reaction entering the coupled Einstein equations, e.g. the source term $\propto \beta(\Phi)e^\Phi T_{MN}^X$ in Eq. (34). In this sense, β_1 is a phenomenological knob for the back-reaction strength (rather than a QCD beta-function coefficient). It does not act as a trivial multiplicative factor on the EoS: even at $\mu = 0$ it changes the full coupled solution and hence modifies the horizon data and the map between T and z_h , leading to a temperature-dependent deformation of dimensionless ratios such as p/T^4 and ϵ/T^4 . Since the horizon probes different dilaton values at different temperatures, the effective back-reaction strength is T dependent, which naturally explains why a single parameter β_1 cannot uniformly fix the curve in all temperature regions within the present ansatz.

To further clarify the impact of β_1 , in Fig. 8 we plot s/T^3 , $3p/T^4$, ϵ/T^4 , and $(\epsilon - 3p)/T^4$ for $\beta_1 = 21, 23, 25$. We see a monotonic increase of s/T^3 , $3p/T^4$ and ϵ/T^4 with β_1 in the whole temperature range shown. The interaction measure $(\epsilon - 3p)/T^4$ is more sensitive around the crossover: increasing β_1 changes the peak region more visibly than the high- T tail. Therefore, tuning only the overall IR magnitude β_1 tends to shift the EoS upward

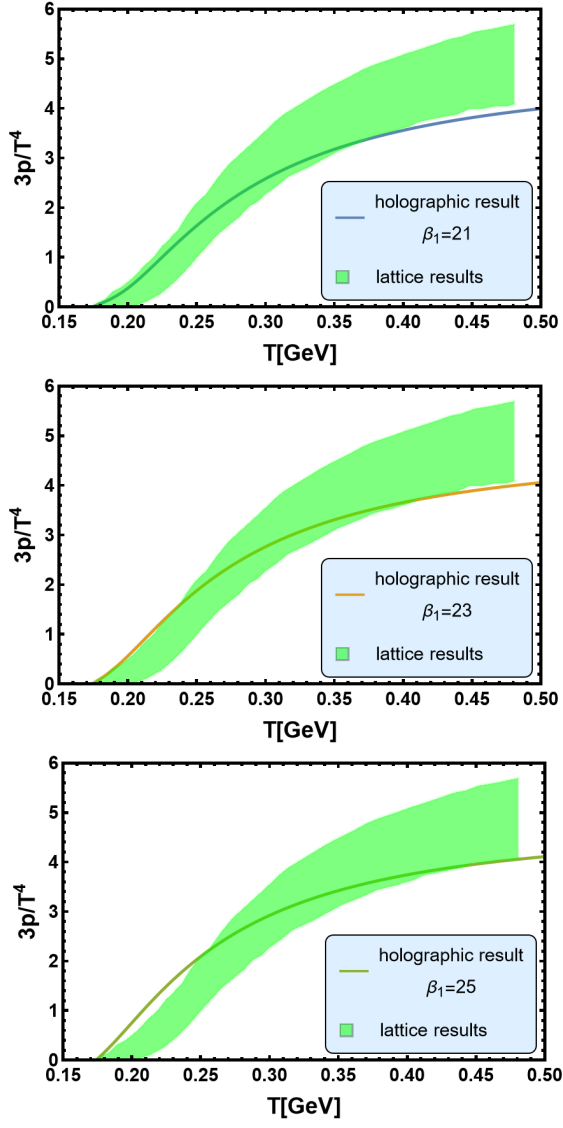


FIG. 7. Coupled EMD+KKSS system with back-reaction at $\mu = 0$: comparison of $3p/T^4$ with the $N_f = 2$ lattice QCD result of Ref. [55] (green band) for three values of the flavor back-reaction strength. Upper: $\beta_1 = 21$; middle: $\beta_1 = 23$; lower: $\beta_1 = 25$. The solid line in each panel is the corresponding holographic result.

in a correlated way across observables, but it does not provide enough freedom to simultaneously match the low- T and high- T parts of the lattice EoS. This suggests that a better quantitative agreement in the back-reacted $N_f = 2$ setup likely requires additional flexibility, e.g. varying the Φ dependence of $\beta(\Phi)$ (parameters β_2, β_3) and/or enlarging the ansatz for V_X .

It is also instructive to examine the high-temperature behavior. As shown in Fig. 9, for sufficiently large T the curves for different values of β_1 approach nearly the same constant (in particular, they approach the $\beta_1 = 0$ curve), while the interaction measure $(\epsilon - 3p)/T^4$ rapidly decays to zero. It is noticed that $\beta_1 = 0$ corresponds to switching

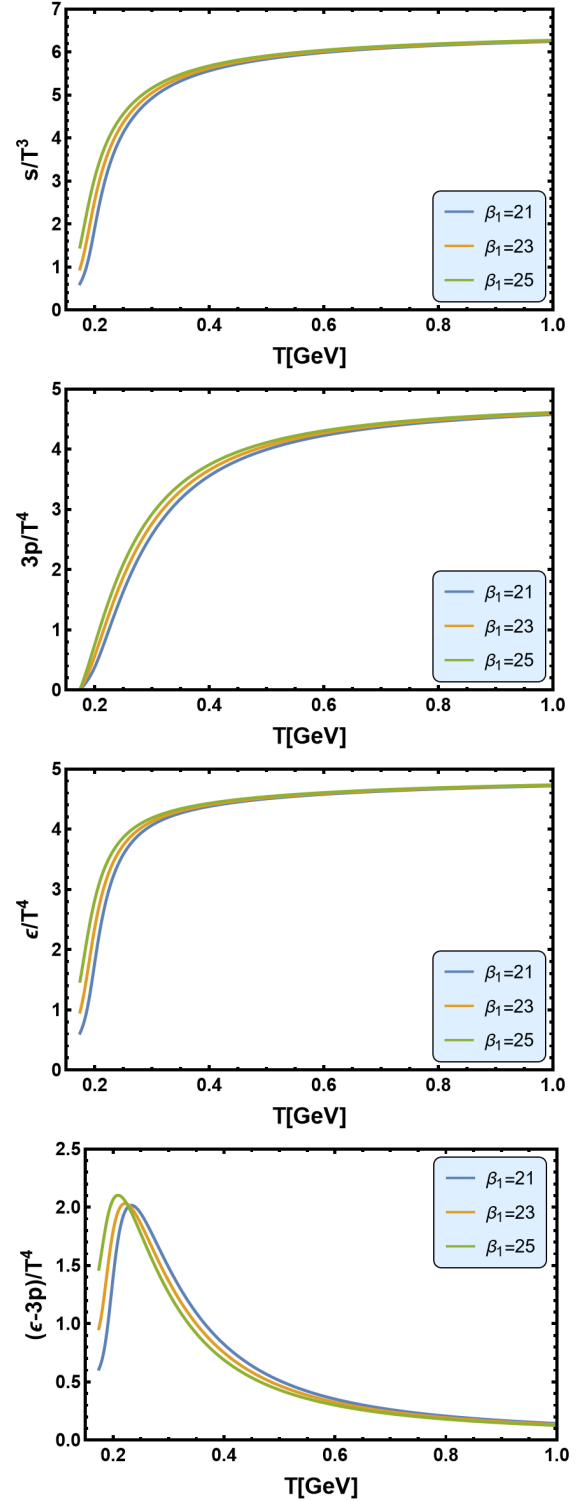


FIG. 8. Dependence on the flavor back-reaction parameter β_1 in the back-reacted $N_f = 2$ study at $\mu = 0$. From top to bottom: s/T^3 , $3p/T^4$, ϵ/T^4 , and $(\epsilon - 3p)/T^4$. In each panel, the three curves correspond to $\beta_1 = 21, 23, 25$, and the horizontal axis is T in units of GeV.

off the flavor coupling, $\beta(\Phi) = 0$, thus it reduces to the pure EMD (pure-gluon, $N_f = 0$) system. This indicates that, within the present truncation of the flavor sector to the χ contribution, the effect of the back-reaction parameter β_1 becomes weak in the high- T region.

This behavior can be understood from the structure of the KKSS action adopted here. In our setup, the flavor sector enters the thermodynamics through $\beta(\Phi)$ and the χ sector, and the polynomial potential V_χ in Eq. (23) does not contain a χ -independent constant term. As a result, in the high- T deconfined region where χ is small and the horizon moves toward the UV, the flavor contribution to the stress tensor (and hence to p/T^4 , s/T^3 , and ϵ/T^4) is suppressed, so the asymptotic plateaus are dominated by the EMD sector that has been fixed by the pure-gluon calibration. This is qualitatively different from the Stefan–Boltzmann (SB) limit of massless QCD, where the pressure receives an $\mathcal{O}(N_c N_f)$ contribution from quark degrees of freedom. For reference, for $SU(N_c)$ with N_f massless quark flavors one has

$$\begin{aligned} \left. \frac{s}{T^3} \right|_{\text{SB}} &= 4 \left. \frac{p}{T^4} \right|_{\text{SB}}, \\ \left. \frac{p}{T^4} \right|_{\text{SB}} &= \frac{\pi^2}{45} (N_c^2 - 1) + \frac{7\pi^2}{180} N_c N_f, \\ \left. \frac{\epsilon}{T^4} \right|_{\text{SB}} &= 3 \left. \frac{p}{T^4} \right|_{\text{SB}}, \\ \left. \frac{\epsilon - 3p}{T^4} \right|_{\text{SB}} &= 0, \end{aligned} \quad (80)$$

Therefore, the fact that our back-reacted curves tend to a β_1 -insensitive plateau in the high- T region provides a simple diagnostic for the present model ansatz: to reproduce the correct high- T flavor contribution, it may be necessary to enlarge the flavor action, e.g. by introducing an additional χ -independent term in the flavor potential (which can be motivated from brane/tension terms in DBI-inspired constructions) and/or by including additional flavor-sector degrees of freedom beyond the χ truncation.

D. Parameter summary

For convenience, we summarize the parameter inputs used in different steps.

VI. CONCLUSION AND OUTLOOK

In this work, we studied the QCD equation of state in a bottom-up holographic framework built from an EMD sector and an improved KKSS flavor sector. The analysis consists of three steps based on the same setup but different approximations. In the probe approximation, we calibrated the EMD model to the lattice EoS of $(2+1)$ -flavor QCD at finite temperature and finite baryon chemical potential by using a neural ODE strategy, and obtained good agreement in the calibrated domain.

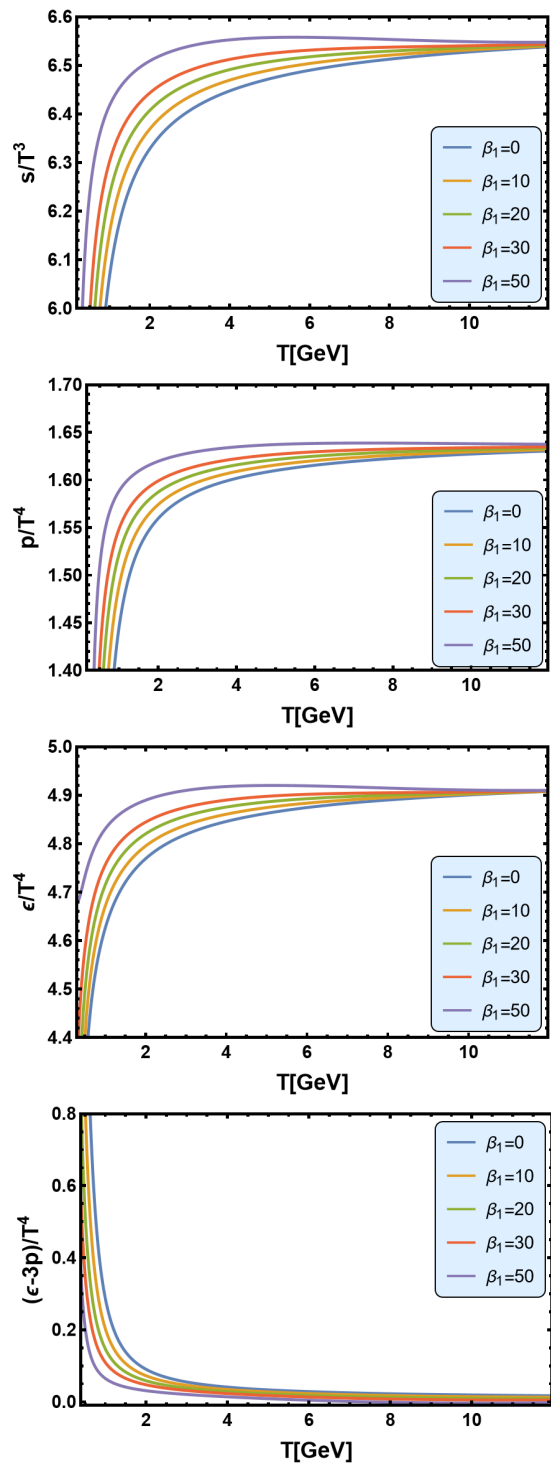


FIG. 9. High-temperature behavior in the back-reacted $N_f = 2$ study at $\mu = 0$ for different values of the flavor back-reaction strength parameter β_1 . From top to bottom: s/T^3 , p/T^4 , ϵ/T^4 , and $(\epsilon - 3p)/T^4$. In each panel, the five curves correspond to $\beta_1 = 0, 10, 20, 30, 50$, and the horizontal axis is T in units of GeV. It is noticed that the curve at $\beta_1 = 0$ corresponds to switching off the flavor coupling, $\beta(\Phi) = 0$, thus it reduces to the pure EMD (pure-gluon, $N_f = 0$) system.

TABLE I. Summary of parameter choices used in different steps. In the probe approximation, $V_\phi(\phi)$ and $h_\phi(\phi)$ are obtained as discrete samples from the neural ODE calibration and then parametrized. In the pure-gluon step, the EMD parameters are fixed by a hybrid optimization. In the back-reacted $N_f = 2$ step, the EMD sector is kept fixed and the KKSS couplings (including the back-reaction strength encoded in $\beta(\Phi)$) are varied for comparison with the lattice EoS.

Sector / step	Key inputs
Probe (2 + 1), finite T, μ	$V_\phi(\phi)$ and $h_\phi(\phi)$ from neural-ODE calibration (Sec. III A); see also Eqs. (66)–(70)
Pure glue, $\mu = 0$	$V_\phi(\phi)$ ansatz in Eq. (73) with $\Delta_\phi = 3.8$; best-fit normalizations (Λ, G_5) in Eq. (75); best-fit potential parameters $(v_0, a_4, a_6, a_8, a_{10})$ in Eq. (76)
Back-reacted $N_f = 2, \mu = 0$	$\beta(\Phi)$ in Eq. (25); g_c in Eq. (22); (λ_2, λ_4) in Eq. (23); $m_u = 24.826$ MeV (fixed by the $m_\pi = 360$ MeV ensemble of Ref. [55] via the GOR relation); and the parameter values used in this work are summarized in Eq. (79)

Treating the EMD system as an effective dual description of pure Yang–Mills theory, we then fixed the EMD parameters by fitting the $\mu_B = 0$ lattice pure-gluon EoS with a hybrid optimization method. Finally, we went beyond the probe approximation and solved the coupled EMD+KKSS equations with back-reaction at $\mu_B = 0$; with the EMD sector fixed by the pure-gluon step, we tuned the KKSS parameters to the lattice EoS of two-flavor QCD, where a visible mismatch remains.

It is noticed that the present mismatch is not only a matter of tuning. With the EMD sector fixed by the pure-gluon calibration, the coupled results at high temperature tend to approach a nearly β_1 -insensitive plateau close to the $\beta_1 = 0$ (pure-gluon) baseline, while $(\epsilon - 3p)/T^4$ rapidly decays toward zero. This provides a simple diagnostic for the present coupled ansatz and indicates that, within the present truncation of the flavor sector to the χ contribution and the polynomial potential in Eq. (23), the high- T flavor contribution in the thermodynamics is suppressed compared with the expectation from QCD. Therefore, the mismatch may have several origins, such as limitations of the current ansatz for $\beta(\Phi)$ and V_X , parameter degeneracy, and missing operators in the bottom-up construction. Possible next moves include:

In particular, the nearly flavor-blind high- T plateau may indicate that the present KKSS-type truncation lacks a χ -independent contribution to the flavor free energy. A natural extension, motivated by the generic structure of DBI/tachyon effective actions (where the tachyon potential typically satisfies $V_f(\chi = 0) = 1$), is to allow a brane-tension-like term in the Einstein-frame flavor potential,

$$V_X^E(\chi, \Phi, F_E^2) = V_0^E(\Phi) + \lambda_2|\chi|^2 + \lambda_4|\chi|^4 + \dots, \quad (81)$$

so that the flavor sector can contribute to the thermodynamics even in the chirally symmetric background ($\chi = 0$), providing an adjustable $\mathcal{O}(N_c N_f)$ component in the pressure/entropy at high temperature. It is worth noting that strongly coupled holography is not expected to coincide with the Stefan–Boltzmann limit, but the high- T behavior does provide a clean diagnostic and constrains admissible flavor-sector completions.

Another closely related issue is the extraction of chiral observables in the present back-reacted setup. Since we adopt a non-integer UV scaling dimension $\Delta_\phi = 3.8$, the near-boundary expansions of the background fields involve fractional powers in z . Through the coupled equations, these fractional-power terms propagate into the UV expansion of the chiral scalar $\chi(z)$ and spoil a clean separation of the integer-power modes. As a result, a naive identification of the chiral condensate with the coefficient of the z^3 term becomes numerically ill-conditioned. A systematic treatment should instead define the condensate from the renormalized canonical momentum (equivalently, from the renormalized on-shell action) by introducing appropriate counterterms at a UV cutoff $z = \epsilon$ and taking $\epsilon \rightarrow 0$. We leave such a holographic-renormalization analysis, as well as the associated chiral transition study, to future work.

- enlarging the functional space of $\beta(\Phi)$ and/or V_X (allowing more terms and/or different IR behaviors);
- allowing for a χ -independent term $V_0^E(\Phi)$ in V_X^E (brane-tension contribution) to tune the high- T flavor plateau;
- adding additional observables to constrain the flavor sector, e.g. chiral condensate and chiral transition;
- performing holographic renormalization for the back-reacted flavor sector to define σ_u from the renormalized canonical momentum in the presence of fractional-power UV asymptotics;
- including susceptibilities and/or more data at small μ in the fitting strategy;
- extending the back-reacted calculation to finite baryon chemical potential.

ACKNOWLEDGMENTS

We thank Maria Paola Lombardo for helpful discussions.

- [1] Heng-Tong Ding, Frithjof Karsch, and Swagato Mukherjee. Thermodynamics of strong-interaction matter from Lattice QCD. *Int. J. Mod. Phys. E*, 24(10):1530007, 2015. doi:10.1142/S0218301315300076.
- [2] Wei-jie Fu. QCD at finite temperature and density within the FRG approach: An overview. 5 2022.
- [3] Juan Martin Maldacena. The Large N limit of superconformal field theories and supergravity. *Adv. Theor. Math. Phys.*, 2:231–252, 1998. doi:10.1023/A:1026654312961.
- [4] Steven S. Gubser and Abhinav Nellore. Mimicking the QCD equation of state with a dual black hole. *Phys. Rev. D*, 78:086007, 2008. doi:10.1103/PhysRevD.78.086007.
- [5] Oliver DeWolfe, Steven S. Gubser, and Christopher Rosen. A holographic critical point. *Phys. Rev. D*, 83:086005, 2011. doi:10.1103/PhysRevD.83.086005.
- [6] Matti Jarvinen. Holographic dense QCD in the Veneziano limit. *EPJ Web Conf.*, 274:08006, 2022. doi:10.1051/epjconf/202227408006.
- [7] Yi Yang and Pei-Hung Yuan. Confinement-deconfinement phase transition for heavy quarks in a soft wall holographic QCD model. *JHEP*, 12:161, 2015. doi:10.1007/JHEP12(2015)161.
- [8] Yi Yang and Pei-Hung Yuan. A Refined Holographic QCD Model and QCD Phase Structure. *JHEP*, 11:149, 2014. doi:10.1007/JHEP11(2014)149.
- [9] David Dudal and Subhash Mahapatra. Thermal entropy of a quark-antiquark pair above and below deconfinement from a dynamical holographic QCD model. *Phys. Rev. D*, 96(12):126010, 2017. doi:10.1103/PhysRevD.96.126010.
- [10] David Dudal and Subhash Mahapatra. Interplay between the holographic QCD phase diagram and entanglement entropy. *JHEP*, 07:120, 2018. doi:10.1007/JHEP07(2018)120.
- [11] Zhen Fang, Song He, and Danning Li. Chiral and Deconfining Phase Transitions from Holographic QCD Study. *Nucl. Phys. B*, 907:187–207, 2016. doi:10.1016/j.nuclphysb.2016.04.003.
- [12] Xin-Yi Liu, Xiao-Chang Peng, Yue-Liang Wu, and Zhen Fang. Holographic study on QCD phase transition and phase diagram with two flavors. *Phys. Rev. D*, 109(5):054032, 2024. doi:10.1103/PhysRevD.109.054032.
- [13] Ying-Ying Li, Xing-Lin Liu, Xin-Yi Liu, and Zhen Fang. Correlations between the deconfining and chiral transitions in holographic QCD. *Phys. Rev. D*, 105(3):034019, 2022. doi:10.1103/PhysRevD.105.034019.
- [14] Renato Critelli, Jorge Noronha, Jacquelyn Noronha-Hostler, Israel Portillo, Claudia Ratti, and Romulo Rougemont. Critical point in the phase diagram of primordial quark-gluon matter from black hole physics. *Phys. Rev. D*, 96(9):096026, 2017. doi:10.1103/PhysRevD.96.096026.
- [15] Joaquin Grefa, Jorge Noronha, Jacquelyn Noronha-Hostler, Israel Portillo, Claudia Ratti, and Romulo Rougemont. Hot and dense quark-gluon plasma thermodynamics from holographic black holes. *Phys. Rev. D*, 104(3):034002, 2021. doi:10.1103/PhysRevD.104.034002.
- [16] Irina Ya. Aref'eva, Alexey Ermakov, and Pavel Slepov. Direct photons emission rate and electric conductivity in twice anisotropic QGP holographic model with first-order phase transition. *Eur. Phys. J. C*, 82(1):85, 2022. doi:10.1140/epjc/s10052-022-10025-5.
- [17] Irina Ya. Aref'eva, Kristina Rannu, and Pavel Slepov. Holographic model for heavy quarks in anisotropic hot dense QGP with external magnetic field. *JHEP*, 07:161, 2021. doi:10.1007/JHEP07(2021)161.
- [18] Rong-Gen Cai, Song He, and Danning Li. A hQCD model and its phase diagram in Einstein-Maxwell-Dilaton system. *JHEP*, 03:033, 2012. doi:10.1007/JHEP03(2012)033.
- [19] Xun Chen, Danning Li, Defu Hou, and Mei Huang. Quarkyonic phase from quenched dynamical holographic QCD model. *JHEP*, 03:073, 2020. doi:10.1007/JHEP03(2020)073.
- [20] Song He, Yi Yang, and Pei-Hung Yuan. Analytic Study of Magnetic Catalysis in Holographic QCD. 4 2020.
- [21] Rong-Gen Cai, Song He, Li Li, and Hong-An Zeng. Neural Ordinary Differential Equations for Mapping the Magnetic QCD Phase Diagram via Holography. *Sci. China Phys. Mech. Astron.*, 69(4):240414, 2026. doi:10.1007/s11433-025-2914-x. URL <https://arxiv.org/abs/2406.12772>.
- [22] Rong-Gen Cai, Song He, Li Li, and Yuan-Xu Wang. Probing QCD critical point and induced gravitational wave by black hole physics. 1 2022.
- [23] Mauricio Hippert, Joaquin Grefa, T. Andrew Manning, Jorge Noronha, Jacquelyn Noronha-Hostler, Israel Portillo Vazquez, Claudia Ratti, Romulo Rougemont, and Michael Trujillo. Bayesian location of the QCD critical point from a holographic perspective. *Phys. Rev. D*, 110(9):094006, 2024. doi:10.1103/PhysRevD.110.094006.
- [24] Liqiang Zhu, Xun Chen, Kai Zhou, Hanzhong Zhang, and Mei Huang. Bayesian inference of the critical end point in a (2+1)-flavor system from holographic QCD. *Phys. Rev. D*, 112(2):026019, 2025. doi:10.1103/wpts-lbtr.
- [25] Xun Chen, Floriana Giannuzzi, and Stefano Nicotri. Data-Driven Refinement of an Analytical Holographic Model for the QCD Phase Transition. 12 2025.
- [26] Joshua Erlich, Emanuel Katz, Dam T. Son, and Mikhail A. Stephanov. QCD and a holographic model of hadrons. *Phys. Rev. Lett.*, 95:261602, 2005. doi:10.1103/PhysRevLett.95.261602.
- [27] Andreas Karch, Emanuel Katz, Dam T. Son, and Mikhail A. Stephanov. Linear confinement and AdS/QCD. *Phys. Rev. D*, 74:015005, 2006. doi:10.1103/PhysRevD.74.015005.
- [28] Danning Li and Mei Huang. Dynamical holographic QCD model for glueball and light meson spectra. *JHEP*, 11:088, 2013. doi:10.1007/JHEP11(2013)088.
- [29] Ricky T. Q. Chen, Yulia Rubanova, Jesse Bettencourt, and David Duvenaud. Neural Ordinary Differential Equations. 6 2018.
- [30] Patrick Kidger. On neural differential equations, 2022. URL <https://arxiv.org/abs/2202.02435>.
- [31] Hong-An Zeng, Lingxiao Wang, and Mei Huang. HoloNet: Toward a Unified Einstein-Maxwell-Dilaton Framework of QCD. 12 2025.
- [32] Xun Chen, Yidian Chen, and Kai Zhou. Data-driven Einstein-dilaton model for pure Yang-Mills thermodynamics and glueball spectrum. *Phys. Rev. D*, 112(12):126025, 2025. doi:10.1103/wyr3-2kc5.
- [33] Xun Chen, Lin Zhang, Danning Li, Defu Hou, and Mei Huang. Gluodynamics and deconfinement phase transition

- under rotation from holography. *JHEP*, 07:132, 2021. doi: 10.1007/JHEP07(2021)132.
- [34] Fei Sun, Kun Xu, and Mei Huang. The Splitting of Chiral and Deconfinement Phase Transitions induced by Rotation. *Phys. Rev. D*, 108(9):096007, 2023. doi: 10.1103/PhysRevD.108.096007. URL <https://arxiv.org/abs/2307.14402>.
- [35] Zhibin Li, Yidian Chen, Danning Li, and Mei Huang. Locating the QCD critical end point through the peaked baryon number susceptibilities along the freeze-out line. *Chin. Phys. C*, 42(1):013103, 2018. doi:10.1088/1674-1137/42/1/013103.
- [36] Xun Chen, Danning Li, and Mei Huang. Criticality of QCD in a holographic QCD model with critical end point. *Chin. Phys. C*, 43(2):023105, 2019. doi:10.1088/1674-1137/43/2/023105.
- [37] Lin Zhang, Chutian Chen, Yidian Chen, and Mei Huang. Spectra of glueballs and oddballs and the equation of state from holographic QCD. *Phys. Rev. D*, 105(2):026020, 2022. doi:10.1103/PhysRevD.105.026020.
- [38] Jin-Yang Shen, Xin-Yi Liu, Jin-Rui Wu, Yue-Liang Wu, and Zhen Fang. Phase structure of 2+1-flavor QCD from an Einstein-dilaton-flavor holographic model. 11 2025.
- [39] Jin-Yang Shen, Xin-Yi Liu, Jin-Rui Wu, Yue-Liang Wu, and Zhen Fang. Toward a holographic realization of the 2+1-flavor QCD phase structure. *Phys. Rev. D*, 112(11):L111504, 2025. doi:10.1103/3plt-wlt7.
- [40] Yidian Chen, Danning Li, and Mei Huang. The dynamical holographic QCD method for hadron physics and QCD matter. *Commun. Theor. Phys.*, 74(9):097201, 2022. doi: 10.1088/1572-9494/ac82ad.
- [41] Danning Li, Song He, Mei Huang, and Qi-Shu Yan. Thermodynamics of deformed AdS₅ model with a positive/negative quadratic correction in graviton-dilaton system. *JHEP*, 09:041, 2011. doi: 10.1007/JHEP09(2011)041.
- [42] Hermann Weyl and Henry L Brose. *Raum-Zeit-Materie [Space-Time-Matter]*. Springer, Berlin, 1921.
- [43] H Weyl and J Ehlers. *Space, time, matter: Lectures on general relativity*. Springer, Berlin, 1993.
- [44] Zhen Fang, Yue-Liang Wu, and Lin Zhang. Chiral phase transition and meson spectrum in improved soft-wall AdS/QCD. *Phys. Lett. B*, 762:86–95, 2016. doi: 10.1016/j.physletb.2016.09.009.
- [45] Zhen Fang, Yue-Liang Wu, and Lin Zhang. Chiral Phase Transition with 2+1 quark flavors in an improved soft-wall AdS/QCD Model. *Phys. Rev. D*, 98(11):114003, 2018. doi:10.1103/PhysRevD.98.114003.
- [46] Zhen Fang, Yue-Liang Wu, and Lin Zhang. Chiral phase transition and QCD phase diagram from AdS/QCD. *Phys. Rev. D*, 99(3):034028, 2019. doi: 10.1103/PhysRevD.99.034028.
- [47] Zhen Fang, Yue-Liang Wu, and Lin Zhang. Octet meson spectra and chiral phase diagram in the improved soft-wall AdS/QCD model. *Phys. Rev. D*, 100(5):054008, 2019. doi:10.1103/PhysRevD.100.054008.
- [48] Lloyd N. Trefethen. *Spectral Methods in MATLAB*. SIAM, Philadelphia, PA, 2000. ISBN 9780898714654. doi:10.1137/1.9780898719598. URL <https://doi.org/10.1137/1.9780898719598>.
- [49] Ahmed Abuali, Szabolcs Borsányi, Zoltán Fodor, Johannes Jahan, Micheal Kahangirwe, Paolo Parotto, Attila Pásztor, Claudia Ratti, Hitansh Shah, and Seth A. Trabulsi. New 4D lattice QCD equation of state: Extended density coverage from a generalized T’ expansion. *Phys. Rev. D*, 112(5):054502, 2025. doi: 10.1103/2dmh-26yh.
- [50] MUSES Collaboration. 4D T’ Expansion Scheme (4D-TEsS) — MUSES documentation. https://musesframework.io/docs/modules/eos_texs_4d/index.html, 2024.
- [51] Donald R. Jones, Matthias Schonlau, and William J. Welch. Efficient Global Optimization of Expensive Black-Box Functions. *J. Glob. Optim.*, 13(4):455–492, 1998. doi:10.1023/A:1008306431147. URL <https://doi.org/10.1023/A:1008306431147>.
- [52] Bobak Shahriari, Kevin Swersky, Ziyu Wang, Ryan P. Adams, and Nando de Freitas. Taking the human out of the loop: A review of bayesian optimization. *Proceedings of the IEEE*, 104(1):148–175, 2016. doi: 10.1109/JPROC.2015.2494218. URL <https://doi.org/10.1109/JPROC.2015.2494218>.
- [53] Jasper Snoek, Hugo Larochelle, and Ryan P. Adams. Practical Bayesian Optimization of Machine Learning Algorithms. In *Advances in Neural Information Processing Systems 25*, pages 2960–2968, 2012. URL <https://proceedings.neurips.cc/paper/2012/hash/05311655a15b75fab86956663e1819cd-Abstract.html>.
- [54] Michele Caselle, Alessandro Nada, and Marco Panero. QCD thermodynamics from lattice calculations with nonequilibrium methods: The SU(3) equation of state. *Phys. Rev. D*, 98(5):054513, 2018. doi: 10.1103/PhysRevD.98.054513.
- [55] Florian Burger, Ernst-Michael Ilgenfritz, Maria Paola Lombardo, and Michael Müller-Preussker. Equation of state of quark-gluon matter from lattice QCD with two flavors of twisted mass Wilson fermions. *Phys. Rev. D*, 91(7):074504, 2015. doi:10.1103/PhysRevD.91.074504.